J. Fluid Mech. (1996), vol. 325, pp. 163–194

A full-scale numerical study of interfacial instabilities in thin-film flows

By B. RAMASWAMY[1], S. CHIPPADA[2] AND S. W. JOO[3]

[1]Department of Mechanical and Environmental Engineering, University of California, Santa Barbara CA 93106-5130, USA

[2]TICAM, University of Texas, Austin, TX 78712, USA

[3]School of Mechanical Engineering, Yeungnam University, Kyongsan, Korea

(Received 4 December 1995)

Surface wave instabilities in a two-dimensional thin draining film are studied by a direct numerical simulation of the full nonlinear system. A finite element method is used with an arbitrary Lagrangian–Eulerian formulation to handle the moving boundary problem. Both temporal and spatial stability analysis of the finite-amplitude nonlinear wave regimes are done. As the wavenumber is decreased below the linear cut-off wavenumber, supercritical sinusoidal waves occur as reported earlier from weakly nonlinear analysis and experiments. Further reduction in wavenumber makes the Fourier spectrum broad-banded resulting in solitary humps. This transition from nearly sinusoidal permanent waveforms to solitary humps is found to go through a quasi-periodic regime. The phase boundaries for this quasi-periodic regime have been determined through extensive numerical parametric search. Complex wave interaction processes such as wave merging and wave splitting are discussed. In the exhaustive numerical simulations performed in this paper, no wave-breaking tendency was observed, and it is speculated that the complex wave-interaction processes such as wave merging and wave splitting curb the tendency of the film to break.

1. Introduction

Interfacial instabilities in thin liquid films draining down inclined or vertical walls have been studied extensively since the seminal work of Kapitza & Kapitza (1949). A vast body of literature exists on the thin-film instability and has been reviewed by Lin & Wang (1985), Chang (1994) and Joo (1995). The earliest theoretical studies into the thin-film instability were based on a hydrodynamic linear stability analysis (Yih 1955, 1963; Benjamin 1957; Whitaker 1964; Anshus & Goren 1966; Krantz & Goren 1971; Pierson & Whitaker 1977; Chin, Abernathy & Bertschy 1986). The basic flat-film solution is unstable to long-wavelength disturbances if the Reynolds number is greater than a certain critical value given by

$$G_c \sin\beta = \tfrac{5}{2}\cot\beta. \tag{1.1}$$

This linear stability result for the cut-off Reynolds number was experimentally verified by Liu, Paul & Gollub (1993). The linearly unstable region is bounded by two neutral curves given by: $k = 0$ and $k = k_c(G, S, \beta)$. Linear stability theory also predicts the wavenumber with the maximum linear growth rate (k_M). In the absence of external periodic forcing, the waves at the point of inception are likely to be of the linear maximum growth rate wavenumber and partial experimental confirmation of this was provided by Alekseenko, Nakoryakov & Pokusaev (1985).

Approximate nonlinear stability theories have been developed to study the evolution subsequent to wave inception. For very thin layers the cut-off wavenumber is small, so that the nonlinear extension of the stability analysis can be accommodated by the small-wavenumber approximation and lubrication theory. By expressing the flow variables as a power series in $\epsilon = h_0/L$, the complicated nonlinear system given by the Navier–Stokes equations can be reduced to a single nonlinear evolution equation for the film thickness $h(x,t)$. Benney (1966) first derived the nonlinear evolution equation for two-dimensional flows accurate up to $O(\epsilon^2)$, but failed to observe any finite-amplitude permanent waves since the stabilizing surface tension appears to the leading order only in the neglected $O(\epsilon^3)$ terms. Weakly nonlinear analysis of the long-wave evolution equation up to various orders of accuracy has been done by Lin (1969), Gjevik (1970) and Nakaya (1975) among others, and they all predict supercritical finite-amplitude permanent waves for wavenumbers slightly lower than the linear cut-off wavenumber k_c in the presence of sufficiently large surface tension. Roskes (1970) extended the long-wave evolution equation of the Benney type to three dimensions. In two dimensions, with the scaling $S \sim O(\epsilon^{-2})$ and $G \sim O(1)$, the long-wave evolution equation for vertically draining thin film is

$$h_t + Gh^2h_x + \epsilon\left[\frac{2G^2}{15}\left(h^6h_x\right)_x + Sh_{xxxx}\right] + O(\epsilon^2) = 0. \tag{1.2}$$

A complete nonlinear numerical solution of the long-wave equation has been obtained by Pumir, Manneville & Pomeau (1983) and Joo, Davis & Bankoff (1991), and they confirm the weakly nonlinear analysis prediction for the supercritical finite-amplitude waves for wavenumbers just below the linear cut-off wavenumber k_c. Further, they predict surface waves of the 'solitary hump' type for wavenumbers much smaller than the linear cut-off wavenumber k_c. For two-dimensional films, Sivashinsky & Michelson(1980) showed that, in the limit of large surface tension ($S \to \infty$), and small wave amplitude ($|h-1| \ll 1$), the evolution equation can be further simplified to the Kuramoto–Sivashinsky equation written as

$$A_t + 2GAA_x + \frac{2G^2}{15}A_{xx} + \tfrac{1}{3}A_{xxxx} = 0, \tag{1.3}$$

where $A = h - 1$ is the amplitude of the surface wave.

For relatively thick layers, the lubrication theory breaks down, because the nonlinear inertia terms are no longer small. In this case, an approximate Karman–Pohlhausen integral boundary layer theory can be used, where a velocity profile is imposed *a priori*. A number of different evolution equations have been derived, depending on the velocity profile imposed. A uniform velocity profile results in the shallow water theory of Dressler (1949). Alekseenko *et al.* (1985) imposed a parabolic profile to derive a more appropriate evolution equation, which was further extended recently by Prokopiou, Cheng & Chang (1991) to higher-order accuracy. In the integral boundary layer theory, a coupled set of two evolution equations is obtained, one for the flow rate $q = \int_0^h u\,\mathrm{d}y$, and the other for the film thickness $h(x,t)$. A parabolic velocity profile results in the following evolution equations:

$$\frac{\partial q}{\partial t} + 1.2\frac{\partial}{\partial x}\left(\frac{q^2}{h}\right) = h\left(G\sin\beta - G\cos\beta\,\frac{\partial h}{\partial x} + 3S\frac{\partial}{\partial x}\left(\frac{1}{R}\right)\right) - 3\frac{q}{h^2}, \tag{1.4a}$$

$$\frac{\partial h}{\partial t} + \frac{\partial q}{\partial x} = 0. \tag{1.4b}$$

With some additional approximations, the above two evolution equations can be combined into one second-order wave equation for the film thickness $h(x,t)$ (Alekseenko *et al.* 1985). Lee & Mei (1996) derived an evolution equation, valid for larger Reynolds numbers and moderate Weber numbers, based on the boundary layer approximation and *a priori* specification of a parabolic velocity profile. Chang, Demekhin & Kopelevich (1993) solved the long-wave boundary layer equations without *a priori* specification of the velocity profiles.

In the majority of the nonlinear studies based on the long-wave boundary layer equations, finite-amplitude permanent waves are assumed *a priori* and the stationary equations are solved in a frame of reference translating with the wave speed c. Chang *et al.* (1993), based on this type of analysis, predict slow-moving short nearly sinusoidal waves referred to as the γ_1 family and fast-moving long solitary waves with one or more primary humps referred to as the γ_2 family. Based on a detailed bifurcation analysis of the third-order dynamical system resulting from the assumption of stationary waves, Lee & Mei (1996) found a variety of bifurcation phenomena, such as limit cycles, heteroclinic orbits, chaotic attractors and homoclinic orbits.

The approximate nonlinear theories discussed above give very good predictions in the parameter ranges in which they are valid. The supercritical nearly sinusoidal waves for wavenumbers slightly lower than the cut-off wavenumber k_c and the subcritical solitary humps for even smaller wavenumbers $k \ll k_c$ as predicted by the approximate nonlinear theories have also been observed experimentally. However, these approximate theories become inaccurate when the wave profile becomes steep thus exciting the higher harmonics, and the long wave, hydrostatic pressure and parabolic velocity profiles are no longer reasonable assumptions. To determine the nonlinear evolution of the thin-film flows without any *a priori* assumptions, the complete Navier–Stokes equations need to be solved. Owing to the irregular and time-varying flow domains involved, the finite element method (FEM) has been the popular method of choice in the direct numerical study of thin-film flows (Bach & Villadsen 1984; Kheshgi & Scriven 1987; Malamataris & Papanastasiou 1991; Salamon, Armstrong & Brown 1994). Ho & Patera (1990) used the Legendre spectral element method, which is a higher-order FEM. Bach & Villadsen (1984), Kheshgi & Scriven (1987) and Malamataris & Papanastasiou (1991) used a Lagrangian FEM to handle the moving boundary and control the mesh distortion through rezoning. Ho & Patera (1990) used a mixed Lagrangian–Eulerian representation to handle the moving boundary and Salamon *et al.* (1994) used the concept of vertical spines.

Kheshgi & Scriven (1987) and Ho & Patera (1990) compare their full-scale numerical results with the Orr–Sommerfeld linear stability results for the neutral wavenumbers. Ho & Patera (1990) obtained good agreement with the experimental results of Kapitza & Kapitza (1949) for the wave profiles and wave speeds. In finite-length domains without any periodic boundary conditions, Kheshgi & Scriven (1987) could not observe any steady travelling waves. However, Malamataris & Papanastasiou (1991) using a modified free boundary condition predicted travelling waves in truncated domains.

Salamon *et al.* (1994) did a comprehensive direct numerical study of travelling waves in vertical thin films and compared their results against the approximate long-wave and boundary layer theories. They assumed *a priori* the existence of steady travelling waves and rewrote the governing equations in a frame of reference translating with the wave speed. They thus solved the steady-state Navier–Stokes equations and computed the flow field, free-surface profile and wave speed simultaneously for a given wavelength and Reynolds number. They found good agreement with the

long-wave theory for small-amplitude waves, but their results qualitatively diverged from the long-wave results for large-amplitude waves. They also studied the nonlinear interactions between the waves and the secondary subharmonic bifurcations to longer waves.

The present numerical study is different from the above-mentioned direct numerical studies in many respects. Firstly, with the exception of Salamon *et al.* (1994), all the previous numerical studies focus on the numerical procedure itself, and validate their approach by comparing with linear theory or experiments. They do not, however, perform a detailed study of the physics of thin-film instability. Salamon *et al.* (1994) do a very detailed study of the thin-film instability. However, they *a priori* assume steady travelling waves and solve the steady-state Navier–Stokes equations in a moving frame of reference. Steady travelling waves are only one of the many possible wave types, and there exist several aperiodic wave motions as well which are investigated and discussed in this paper. We also do the spatial stability analysis by taking a very long domain and imposing time-periodic disturbances at the inlet. This is usually the way stability is investigated in experiments, thus permitting us to make direct quantitative comparison between full-scale computations and experiments. This type of spatial stability study via full-scale computations has not been attempted previously to our knowledge.

Experimental studies of falling films have been done by, among others, Kapitza & Kapitza (1949), Krantz & Goren (1971), Portalski & Clegg (1972), Alekseenko *et al.* (1985), and Lacy, Scheintuck & Dukler (1991). As summarized by Alekseenko *et al.* (1985), in most of the experiments performed, two-dimensional regular waves are observed only near the wave-inception line. The waves soon become three-dimensional and irregular. In order to obtain two-dimensional wavetrains, the flow was disturbed at a fixed frequency by, for example, wire vibrations (Krantz & Goren 1971) and pulsations of flow rate (Kapitza & Kapitza 1949; Alekseenko *et al.* 1985). Lacy *et al.* (1991) performed the experiments without artificial perturbations, and noticed that draining films exhibit deterministic chaos. More recent experiments have been performed by Liu *et al.* (1993) and Liu & Gollub (1993, 1994) on an inclined plane surface to study the primary and secondary instabilities and solitary wave dynamics of film flow. Liu *et al.* (1993) measured the primary surface wave instabilities and found good agreement with the linear stability predictions for the cut-off Reynolds number, growth rates and wave velocities. Good experimental agreement with the linear theory has also been found by Knani & Bankoff (1993). Liu *et al.* also showed the primary instability to be convective in character and hence extremely sensitive to external noise at the source. Liu & Gollub (1993) found the primary surface wave instability to be susceptible to both sideband and subharmonic secondary instabilities but in different ranges of frequency. Liu & Gollub (1994) performed a systematic analysis of solitary wave dynamics in two dimensions and found the velocity of the solitary wave to be proportional to the wave height. Thus the bigger wave travels faster and coalesces in an inelastic manner with the smaller waves leaving behind a long flat interface.

In this paper, the surface wave instabilities on isothermal thin-film flows draining down inclined or vertical walls are studied through the direct numerical solution of the initial value problem posed by the Navier–Stokes equations. The numerical method employed is the FEM and the free boundary problem is modelled through a mixed Lagrangian–Eulerian procedure called the ALE formulation. The mathematical system including the boundary conditions is described in §2 and the numerical procedure is briefly outlined in §3. In §4, comparisons are made with the experiments

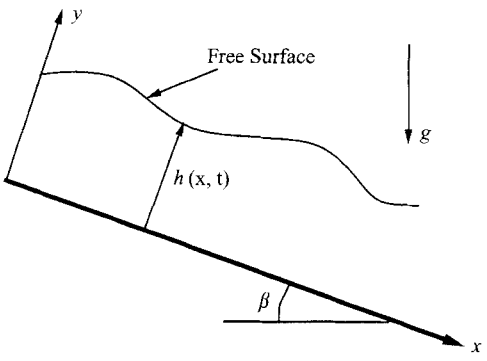

FIGURE 1. Thin liquid film draining down an inclined plane: Problem definition

of Kapitza & Kapitza (1949) and previous numerical simulations of Ho & Patera (1990) and Salamon *et al.* (1994). The nonlinear evolution of the thin film in spatially periodic domains with various wavenumbers and Reynolds numbers is studied in detail in §5. In §6, the spatio–temporal evolution of the thin-film flow is studied by considering very long periodic and non-periodic domains. The findings of our full-scale numerical study are discussed in conjunction with what is already known about thin-film instability based on the approximate linear and nonlinear theories and experimental studies.

2. Formulation

We consider a two-dimensional thin liquid film draining down a planar rigid plate inclined at an angle β to the horizontal as shown in figure 1. The x-axis is aligned along the wall, and the y-axis perpendicular to the wall. The film thickness varies with location and time and is represented by $h(x,t)$. We focus on laminar incompressible Newtonian and isothermal film flows, and write the Navier–Stokes equations and the continuity equation as

$$u_t + uu_x + vu_y = -p_x + G\sin\beta + (u_{xx} + u_{yy}), \tag{2.1a}$$

$$v_t + uv_x + vv_y = -p_y - G\cos\beta + (v_{xx} + v_{yy}), \tag{2.1b}$$

$$u_x + v_y = 0, \tag{2.1c}$$

where the length and time scales are chosen to be the mean film thickness h_0 and the viscous time scale h_0^2/ν, respectively; ν is the kinematic viscosity of the liquid film. The non-dimensional parameter G:

$$G = \frac{gh_0^3}{\nu^2},$$

is some times called the Galileo number, where g is the gravity. A different non-dimensional number $Re = \bar{u}h_0/\nu$ results if the average velocity based on the Nusselt flat film solution $\bar{u} = gh_0^2\sin\beta/(3\nu)$ is used in the non-dimensionalization. Re and G are related as follows:

$$Re = \frac{G\sin\beta}{3}$$

Thus, $G\sin\beta$ can be considered as the Reynolds number Re.

On the bottom plate the no-slip and impermeability conditions are to be imposed:

$$u = v = 0 \quad \text{at } y = 0. \tag{2.2}$$

The dynamics of the gaseous phase are neglected. The boundary conditions at the free surface are the zero-shear-stress condition,

$$(u_y + v_x)(1 - h_x^2) - 4u_x h_x = 0, \tag{2.3}$$

the normal-stress condition,

$$p - \frac{2[u_x(h_x^2 - 1) - h_x(u_y + v_x)]}{(1 + h_x^2)} = -\frac{3Sh_{xx}}{(1 + h_x^2)^{3/2}}, \tag{2.4}$$

and the kinematic condition,

$$h_t + uh_x = v. \tag{2.5}$$

The non-dimensional parameter S is a measure of the surface tension, and is given by

$$S = \frac{\sigma h_0}{3\rho v^2} \tag{2.6}$$

where σ is the surface tension coefficient and ρ is the density of the liquid.

3. Numerical procedure

The numerical procedure employed to solve the mathematical system described in the previous section is briefly outlined next. The most difficult aspect of this problem is the presence of the *a priori* unknown moving boundary. A mixed Eulerian–Lagrangian description of flow is used which combines the advantages of the pure Eulerian and pure Lagrangian approaches. The mathematical equations are rewritten in the Arbitrary Lagrangian Eulerian (ALE) formulation. In this formulation, the numerical grid points move independently of the fluid particles. The ALE formulation has been used in the solution of several free-surface problems (e.g. Amsden & Hirt 1973; Hirt, Amsden & Cook 1974; Chan 1975; Pracht 1975; Hughes, Liu & Zimmerman 1981; Ramaswamy & Kawahara 1987*b*; Huerta & Liu 1988; Soulaïmani *et al.* 1991) and of fluid–structure interaction problems (e.g. Donea, Giuliani & Halleux 1982; Donea 1983; Belytschko & Flanagan 1982; Liu *et al.* 1988). The mathematical system given by (2.1) is rewritten in the ALE formulation as follows:

$$u_t + (u - w^x)u_x + (v - w^y)u_y = -p_x + G\sin\beta + u_{xx} + u_{yy}, \tag{3.1a}$$

$$v_t + (u - w^x)v_x + (v - w^y)v_y = -p_y - G\cos\beta + v_{xx} + v_{yy}, \tag{3.1b}$$

$$u_x + v_y = 0; \tag{3.1c}$$

w^x and w^y are the mesh point velocities in the x- and y-directions respectively. The boundary conditions remain the same in the ALE formulation. By judicious choice of w^x and w^y very large deformations can be handled and at the same time a sharp gas–liquid interface can be maintained. The representation of the free surface as a height function $h(x, t)$ makes this very easy. The free surface is parameterized by vertical spines equally spaced in the x-direction. Along each vertical spine a predetermined number of grid points is assigned and distributed depending on the location of the free surface. Thus the mesh points only slide up and down along the vertical spines and do not move in the horizontal direction ($w^x = 0$), thus eliminating the problem of mesh distortions which are common in pure Lagrangian approaches.

On the free surface there are three boundary conditions that need to be satisfied: (2.3), (2.4) and (2.5). In the numerical solution of the Navier–Stokes equations two boundary conditions are sufficient and the third one is used to update the location of the free surface every time step. The stress conditions are imposed in the solution of the Navier–Stokes equations and the kinematic free-surface condition is used to update the free-surface location. Moreover, the kinematic condition is numerically solved in an alternative equivalent form given by

$$h_t + Q_x = 0 \tag{3.2}$$

where $Q = \int_0^{h(x,t)} u\,dy$ is the volumetric flow rate. If the spatial domain is periodic in the streamwise direction, the above one-dimensional equation is integrated in time using the second-order-accurate Leap Frog scheme and the spatial derivatives are computed using the Fourier spectral method (FSM). If the spatial domain is non-periodic in the streamwise direction, the kinematic condition is integrated in time using the second-order-accurate Adams–Bashforth scheme and the spatial derivatives are computed using the central differences finite difference method (FDM).

The various steps involved in calculating the flow field and mesh point location $(u^{n+1}, v^{n+1}, p^{n+1}, x^{n+1}, y^{n+1}, h^{n+1})$ at the next time level, knowing the flow field and mesh point location $(u^n, v^n, p^n, x^n, y^n, h^n)$ previous time level is described next. The first step in each time step calculation involves finding the new free-surface location h^{n+1} using the previous time level free-surface height h^n and velocity field u^n. Knowing the new time level free-surface height h^{n+1}, the grid points are redistributed along the vertical spines in an equi-spaced manner. Since the grid points move only along the vertical spines, $x^{n+1} = x^n$ and $w^x = 0$. The mesh velocities in the y-direction are calculated as: $w^y = \left(y^{n+1} - y^n\right)/\Delta t$, where Δt is the time step size. Knowing the updated mesh point locations (x^{n+1}, y^{n+1}) and mesh point velocities (w^x, w^y) the velocity and pressure field is calculated next. The continuity equation (3.1*c*) is replaced by an equivalent pressure Poisson equation, and the fractional step method, first proposed by Chorin (1967) is used for the time discretization of the Navier–Stokes equations (3.1). The pressure gradients are dropped from (3.1*a*, *b*) and approximate velocities not necessarily divergence free are computed first. The pressure gradient terms are then added back to these approximate velocities in such a way that the final velocities are divergence free. The fractional step method which is also called the projection method, or the velocity correction method is being increasingly used in the numerical solution of the Navier–Stokes equations (e.g. Chorin 1967; Temam 1971; Patankar 1980; Pironneau 1982; Donea, Giuliani & Laval 1982; Mizukami & Tsuchiya 1984; Kim & Moin 1985; Kawahara & Ohmiya 1985; Van Kan 1986; Glowinski 1986; Bell, Colella & Glaz 1989; Gresho 1990; Gresho & Chan 1990; Le & Moin 1991; Oden 1992; Finlayson 1992; Ramaswamy, Jue & Akin 1992). The fluid domain is spatially discretized through three-node triangular elements and equal-order approximation for velocity and pressure is used. The equal-order approximation for the velocity and pressure (also called the non-staggered grid) has been used by several researchers in the numerical solution of the Navier–Stokes equations (e.g. Schneider, Raithby & Yovanovich 1978; Rice & Schnipke 1986; Ramaswamy & Kawahara 1987*a*; Shaw 1991; Zienkiewicz & Wu 1991, 1992; Behr, Franca & Tezduyar 1992; Gresho *et al.* 1994).

Most of the results to be reported later used 11 points in the y-direction. In the x-direction the number of mesh points varied from as small as 65 to as large as 2001 depending on the length of the domain. Where possible, mesh-independent tests have been performed.

4. Comparison with experiments and previous full-scale numerical studies

Kapitza & Kapitza (1949) obtained two-dimensional permanent waves on thin films draining down a cylinder by artificially perturbing the flow rate at a fixed frequency and amplitude. Ho & Patera (1990) and Salamon *et al.* (1994) compared their full-scale numerical results with the experimental findings of Kapitza & Kapitza (1949) for the two conditions listed in table 1. These two experimental conditions are numerically simulated through our full-scale numerical procedure and compared with the experimental results of Kapitza & Kapitza (1949), Ho & Patera (1990) and Salamon *et al.* (1994).

What is investigated in experiments is the spatial stability, where a periodic disturbance is imposed at the inlet and its evolution in the streamwise direction is determined. For periodic forcing at the inlet, sufficiently far downstream from the inlet Kapitza & Kapitza (1949) observed saturation of the disturbance and the waves travel downstream with fixed wave speed and wavelength. Numerically, however, the equilibrium wave profile and wave speed are obtained through temporal stability analysis. A streamwise-periodic disturbance with wavelength λ as obtained in the experiments is imposed as follows:

$$h(x,0) = 1 + \delta\cos(kx), \tag{4.1}$$

and its evolution in time is computed through the direct numerical solution of the full nonlinear system given by (3.1). $k = 2\pi h_0/\lambda$ is the non-dimensional wavenumber, and the boundary conditions in the streamwise direction are

$$\phi(x=0) \;=\; \phi(x=\lambda), \tag{4.2}$$

where ϕ stands for h, u, v and p. Saturation of the disturbance in time implies steady travelling waves with fixed wave speed and wave profile. These numerically computed wave profile and wave speed are then compared with those obtained by Kapitza & Kapitza (1949). To start our numerical calculations, we need to specify the mean film thickness. However, Kapitza & Kapitza (1949) do not provide the mean film thickness, and instead give the flow rate. Using the experimental flow rate Q, the mean Nusselt film thickness h_0 is computed as

$$h_0 = \left(\frac{3\nu Q}{g}\right)^{1/3}. \tag{4.3}$$

This mean film thickness is then used to compute the non-dimensional parameters G, S and k. In the numerical formulation, the mean film thickness remains fixed in time, but the flow rate could vary with time. In fact, with the onset of wave motion, the flow rate increases, and the final steady flow rate in our numerical simulation would be greater than the experimental flow rate. The results of the nonlinear evolution are presented in terms of the film thickness $h(x,t)$ at various instants of time and the spatial spectral coefficients $c_n(t)$, defined as

$$h(x,t) = \sum_{n=-N}^{n=N} c_n(t)\mathrm{e}^{\mathrm{i}nkx},$$

where $2N$ is the number of mesh divisions in the streamwise direction. The initial amplitude of the disturbance is set to $\delta = 0.05$.

The nonlinear flow evolution for the experimental condition, namely $G = 18.2$, $S = 463.7$, $\beta = \pi/2$ and $k = 0.07$, is shown in figure 2. The experimental wavenumber $k = 0.07$ is smaller than the linear cut-off wavenumber $k_c = 0.29$ (Whitaker

Fluid	σ/ρ (cm^3 s^{-2})	λ (cm)	Q (cm^2 s^{-1})	G	S	k
alcohol at 16.8°C	29	1.77	0.123	18.2	463.7	0.07
water at 19.6°C	74	0.80	0.201	60.0	4410	0.14

TABLE 1. Experimental conditions of Kapitza & Kapitza(1949) and the relevant non-dimensional parameters.

1964). The wave amplitude thus grows exponentially initially (figure 2*a*). Eventually, however, owing to the stabilizing capillary force, the growth is arrested, resulting in steady travelling waves (figure 2*b*). The dynamics of the nonlinear processes can be better quantified through the spatial spectral coefficients $c_n(t)$ (figure 2*c*). The fundamental mode and its first few harmonics grow exponentially initially. Eventually, owing to the nonlinear stabilizing, they saturate in time, resulting finite-amplitude permanent waves travelling downstream at fixed wave speed c. The equilibrium wave profile obtained using the present method is compared with that reported by Kapitza & Kapitza (1949), Ho & Patera (1990) and Salamon *et al.* in figure 3. It is in good agreement with the measured wave profile of Kapitza & Kapitza (1949) and the numerically computed wave profiles of Ho & Patera (1990) and Salamon *et al.* (1994). The dominant crest has a teardrop profile with a sharp downstream slope and a long gently sloping tail. The sharp hump is preceded immediately downstream by small capillary waves. The free-surface profile is 'solitary wave' type and corresponds to the 'single wave' observed by Kapitza & Kapitza (1949) for wavenumbers much smaller than the cut-off wavenumber k_c. The computed wave speed is 23.1 cm s^{-1} which compares very well with the wave speed of 23.5 cm s^{-1} reported by Salamon *et al.* (1994) and 24.7 cm s^{-1} reported by Ho & Patera (1990). The experimental wave speed reported by Kapitza & Kapitza (1949) is 19.5 cm s^{-1} which is appreciably lesser than the numerically computed wave speeds. As pointed out by Ho & Patera (1990) and Salamon *et al.* (1994), the experimental flow rate is imposed only as an initial condition in the numerical simulation, but owing to the onset of wave motion, there is an increase in the flow rate. Salamon *et al.* (1994) obtained better agreement with the experimental results when they adjusted their mean film thickness to take into account this aspect.

The evolution of the initially imposed sinusoidal perturbation with amplitude 0.05 for the case $G = 60.0$, $S = 4410.0$, $\beta = \pi/2$ and $k = 0.14$ is shown in figure 4. The wavenumber $k = 0.14$ is smaller than the linear cut-off wavenumber $k_c \approx 0.30$. The wave amplitude grows exponentially initially (figure 4*a*). Unlike in the previous case however, the harmonic modes do not saturate in time (figure 4*c*). The spectral coefficients continuously oscillate in time, generating a quasi-periodic waveform†. The fundamental mode and its harmonics are continuously exchanging energy, without settling down to a stationary value. In fact, the total energy of the system defined as

$$E(t) = \sum_{n=-N}^{n=N} |c_n(t)|^2, \tag{4.4}$$

† Quasi-periodicity is often used to mean superposition of two irrationally related periodic oscillations. In this paper however, we use it in a more general sense, i.e. it is used to refer to wave motion that is roughly oscillatory but not singly periodic. Consequently, the wave motion classified as quasi-periodic motion in this paper may have more than two irrationally related periodic oscillations and may be chaotic as well.

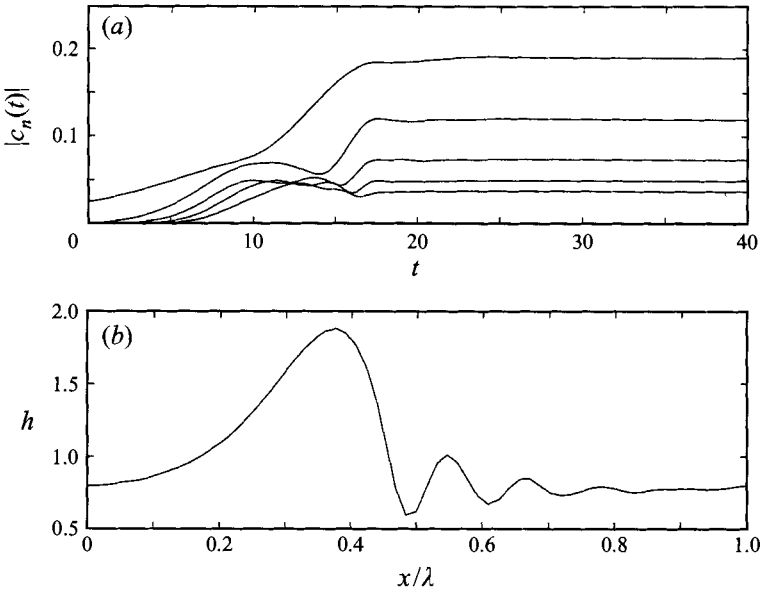

FIGURE 2. $G = 18.2$, $S = 463.7$, $k = 0.07$, $\beta = \pi/2$: (*a*) evolution of the spatial spectral coefficients $|c_n(t)|$; and (*b*) shape of the permanent travelling wave.

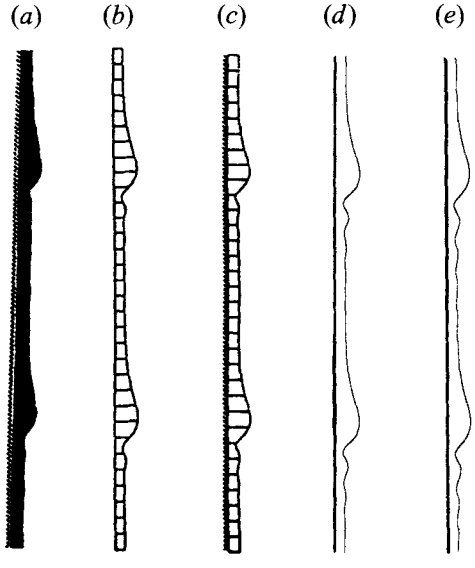

FIGURE 3. Permanent waveform for the case $G = 18.2$, $S = 463.7$, $k = 0.07$, $\beta = \pi/2$: (*a*) Kapitza & Kapitza (1949), (*b*) Salamon *et al.* (1994), (*c*) Ho & Patera(1990), (*d*) Present numerical method; and (*e*) integral boundary layer theory.

was itself found to be continuously oscillating in time. The wave profiles at the two extremes, namely when the fundamental mode has the minimum energy ($t = 77.75$) and when the fundamental mode has the maximum energy ($t = 78.90$) are shown in figure 4(*b*). These two wave profiles along with the steady wave profiles obtained by other researchers are shown in figure 5. The experimental wave profiles and the

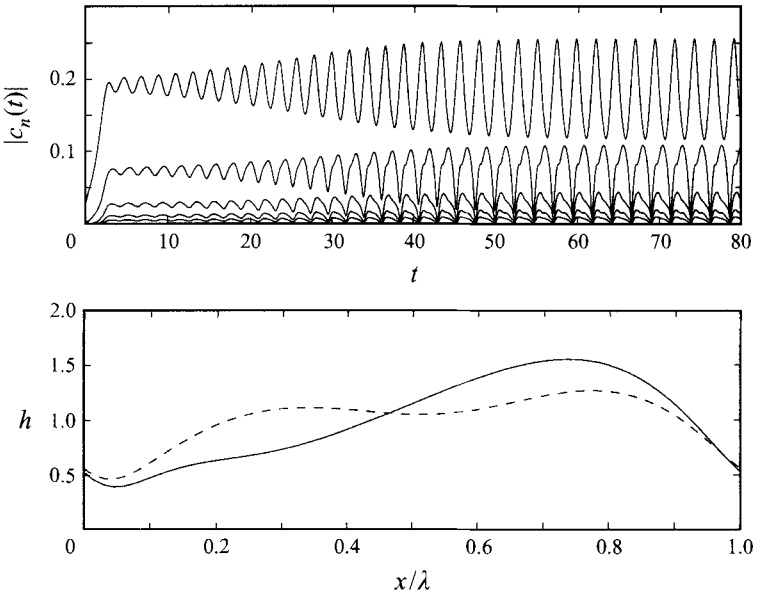

FIGURE 4. $G = 60.0$, $S = 4410.0$, $k = 0.14$, $\beta = \pi/2$: (*a*) evolution of the spatial spectral coefficients $|c_n(t)|$; and (*b*) film thickness at $t = 77.75$ (broken line) and $t = 78.90$ (continuous line).

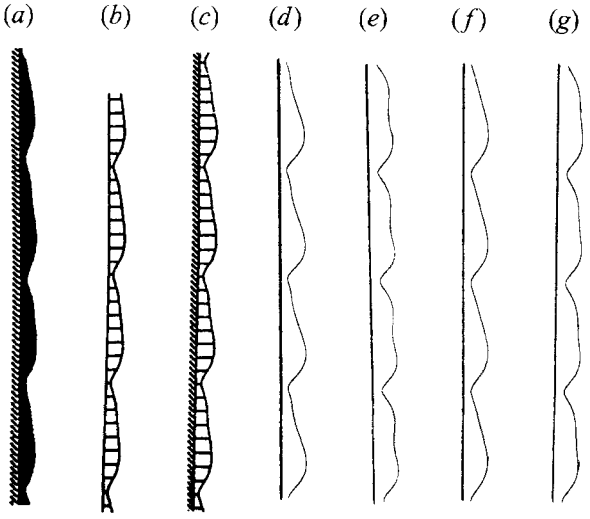

FIGURE 5. Permanent waveform for the case $G = 60.0$, $S = 4410$, $k = 0.14$, $\beta = \pi/2$: (*a*) Kapitza & Kapitza (1949), (*b*) Salamon *et al.* (1994), (*c*) Ho & Patera (1990), (*d*) Present numerical simulation at $t = 77.75$, (*e*) present numerical simulation at $t = 78.90$; and (f,g) integral boundary layer theory.

previously reported numerical wave profiles agree better with the wave profile at $t = 78.90$.

To summarize, for the first experimental condition (figure 2), we obtain a steady travelling waveform with solitary hump shape, and both the wave profile and wave speed are in good agreement with those reported previously. For the second experimental condition, however, our full-scale computations predict a quasi-periodic waveform in contrast to the stationary waveforms reported previously. Recent exper-

iments of Liu & Gollub (1994) also indicate this type of quasi-periodic behaviour. In certain ranges of frequencies they could not observe saturated waves. This quasi-periodic behaviour is investigated in detail in the next section. Assuming for the moment that our numerical results are correct, it remains to be explained why Kapitza & Kapitza (1949), Ho & Patera (1990) and Salamon *et al.* (1994) did not observe this type of a behaviour. Since the wave profiles are not necessarily sinusoidal Kapitza & Kapitza (1949) defined the wave amplitude α as

$$\alpha = \frac{h_{max} - h_{min}}{h_{max} + h_{min}}, \tag{4.5}$$

where h_{max} and h_{min} are respectively the maximum film thickness and the minimum film thickness. The wave amplitudes for different flow rates are given in figure 13 of Kapitza & Kapitza (1949). The second experimental condition simulated by us corresponds to $Q = 0.201$ cm^2 s^{-1}, and for this flow rate they give two wave amplitudes, possibly because they did not observe well-defined stationary travelling waves. The other possibility is that their test section is not long enough for them to be able to observe well-defined quasi-periodic behaviour. From figure 4(*c*), we find that the system needs about 40 non-dimensional time units for the onset of quasi-periodic behaviour. Based on our non-dimensionalization this works out to be $t = 1.34$ s, and at a wave speed of 19.7 cm s^{-1} it would be approximately 26 cm before well defined quasi-periodic behaviour can be observed. The length of the test section used by Kapitza & Kapitza (1949) is only 17 cm.

5. Temporal stability analysis

From the previous section, it appears that for wavenumbers smaller than the linear cut-off wavenumber k_c, we do not always obtain steady travelling permanent waveforms. A similar result was shown experimentally by Liu & Gollub (1994). For excitation frequencies ω closer to the linear cut-off frequency ω_c, they observed nearly sinusoidal saturated waves. As the frequency is reduced, however, in certain ranges of frequencies they observed quasi-periodic evolution in the downstream direction. The film thickness is however still periodic in time, but does not saturate in the streamwise direction. For much smaller wavenumbers, they observed steady travelling solitary waves. Thus, experimental evidence exists for quasi-periodic travelling waveforms. The experimentally investigated thin-film stability is a spatial one, where a periodic disturbances is imposed at the inlet. Our full-scale computations, from the previous section, tell us that this type of quasi-periodic travelling waves is also observed in the temporal stability analysis. The quasi-periodic behaviour was also observed by Hooper & Grimshaw (1985) in their solutions of the Kuramoto–Sivashinsky (KS) equation and by Joo & Davis (1992) in their numerical solutions of the long-wave evolution equation. Hooper & Grimshaw (1985) observed that for some wavenumbers the fundamental mode and its first harmonic are in a 'bouncy state', with continuous exchange of energy between them. Our own numerical solution of the integral boundary layer equations with the assumption of a parabolic velocity profile also indicate that this type of quasi-periodic behaviour is exhibited. A detailed temporal stability analysis of the thin-film flow is thus undertaken in this section to obtain the phase boundaries for this quasi-periodic waveforms.

The long-time behaviour of the system is uniquely determined by G, S, β and k. The non-dimensional number S can be written as $S = TG^{1/3}$, where the new parameter T depends only on the fluid properties. We set $\beta = \pi/2$ and $T = 100$, and

focus on fluids with moderate surface tension. Temporal stability is investigated for G up to 100. For each G, sinusoidal disturbances with amplitude $\delta = 0.05$ and various wavenumbers are imposed and their evolution in time is followed by the integration of the full-scale system (3.1), subject to the boundary conditions (2.2), (2.3), (2.4), (4.2). The temporal stability results for $G = 5, 25$ and 100 and $k = k_M, k_M/2$ and $k_M/4$ are first presented. The linear maximum growth rate wavenumber k_M for the system is taken to be that given by Whitaker (1964) based on the numerical solution of the Orr–Sommerfeld equation.

In figure 6, the evolution for $G = 5$ is shown for three wavenumbers, 0.10, 0.05 and 0.025. The harmonic modes undergo very complicated interactions for smaller k. However, they eventually saturate for all three wavenumbers, resulting in finite-amplitude permanent waves travelling downstream with a fixed wave speed. The harmonic content becomes broad-banded as the wavenumber is reduced, resulting in a 'solitary wave', preceded downstream by capillary ripples (figure 6*d*). Further reduction in wavenumber results in more than one solitary pulse (figure 6*f*). Thus, very far away from the inlet, a solitary waveform is the preferred wave shape, and moreover, there appears to be a natural nonlinear wavelength that the system chooses to have. This natural nonlinear wavelength is different from the maximum growth rate wavelength λ_M predicted by linear theory. Also shown in figure 6 are the final permanent waveforms predicted by the long-wave evolution equation of the Benney type (1.2). The agreement between the two is found to be very good, even though the long-wave theory over-predicts the full-scale numerical solution.

The nonlinear evolution of the spatial harmonic coefficients $c_n(t)$ and the final permanent waveform for $G = 25$ and $k = 0.30$, 0.15 and 0.075 are shown in figure 7. The initial exponential growth is followed by equilibration of the modes for all the three wavenumbers, resulting in finite-amplitude permanent waveforms travelling downstream with fixed wave speed on the gas–liquid interface. The notable difference from the $G = 5$ case is the substantially larger wave amplitude with the maximum wave height more than double the mean film thickness for the wavenumber $k = 0.075$ (figure 7*f*). As the wavenumber is reduced the waveform changes from nearly sinusoidal waves to broad-banded solitary waves. Attempts to solve the long-wave evolution equation of the Benney type for $G = 25$ have resulted in numerical breakdown for all three wavenumbers. This is not very surprising since it is valid only for $G \sim O(1)$. The approximate integral boundary layer theory (1.4) valid for moderate Reynolds number is solved and the resulting wave profiles are plotted in figure 7(*b*, *d*, *f*). We obtain excellent agreement between the full-scale computations and the integral boundary layer theory in this case.

The nonlinear evolution of the harmonic coefficients for the case $G = 100$ and $k = 0.40$, 0.20 and 0.10 are shown in figure 8. For $k = 0.4$, the harmonic modes undergo complex nonlinear interactions. However, unlike those seen previously for $G = 5$ and $G = 25$, the harmonic modes do not saturate in time. Rather, they are oscillating in time, with continuous transfer of energy between the modes, which is also seen in the previous section (figure 4). This corresponds to a quasi-steady waveform and we do not observe a steady permanent waveform. A similar but more complex time behaviour is observed in the case of $k = 0.20$ (figure 8*c*). The wave profiles shown in figure 8(*b*, *d*) are consequently not the final permanent waveforms, but are the wave shape at a particular instant of time. However, for $k = 0.10$ ($\approx k_M/4$), the harmonic modes eventually saturate (figure 8*e*), and the final permanent waveform (figure 8*f*) is solitary wave-like with a primary teardrop hump preceded downstream by several capillary ripples. Attempts to solve the integral boundary layer system

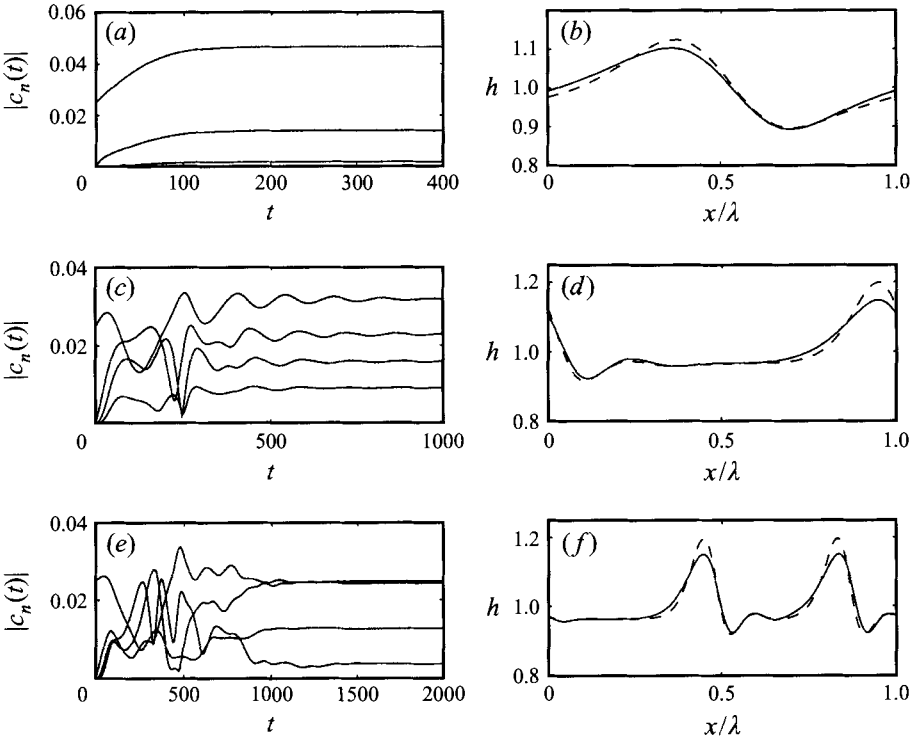

FIGURE 6. $G = 5.0$, $T = 100$, $\beta = \pi/2$: (*a*) evolution of the spectral coefficients for $k = 0.10(\approx k_M)$; (*b*) permanent wave profile for $k = 0.10(\approx k_M)$; (*c*) evolution of spectral coefficients for $k = 0.05(\approx k_M/2)$; (*d*) permanent wave profile for $k = 0.05$ ($\approx k_M/2$); (*e*) evolution of spectral coefficients for $k = 0.025$ ($\approx k_M/4$); (*f*) permanent wave profile for $k = 0.025$ ($\approx k_M/4$). The wave profiles obtained using the longwave theory are shown in broken lines.

(1.4) have failed. This is surprising, since $G = 100$ can still be considered as moderate Reynolds number. We think that the difference is due to the small surface tension parameter, namely $T = 100$. Significant wave steepening is observed in this case and the parabolic velocity profile and hydrostatic pressure assumptions may no longer be valid. The integral boundary layer theory of Lee & Mei (1995) is valid for large Reynolds number and moderate surface tension and may not encounter this problem.

Before we proceed further, it will be worthwhile to look at the wave profiles at different instants of time to understand what is happening physically during the quasi-periodic evolution. The wave profiles at different times for the case $G = 100$ and $k = 0.20$ are shown in figure 9. For clarity the free-surface profiles are shown over a three-wavelength domain. Particularly noteworthy is the growth of the subsidiary peak just upstream of the primary wave and its coalescence with the primary wave. At the end of this coalescence there are only three subsidiary peaks between any two primary humps. Very soon a new subsidiary peak develops and starts growing and merges with the primary maxima and the process is repeated. It is this phenomenon which results in the fluctuations of the harmonic modes and multiple periodic states wave profiles. This particular phenomenon of the growth of the subsidiary peak and its merger with the primary hump has also been observed experimentally by Liu & Gollub (1994). Thus, in the transition from nearly sinusoidal permanent waves to a solitary wave train there exists a band of wavenumbers (frequencies) where the

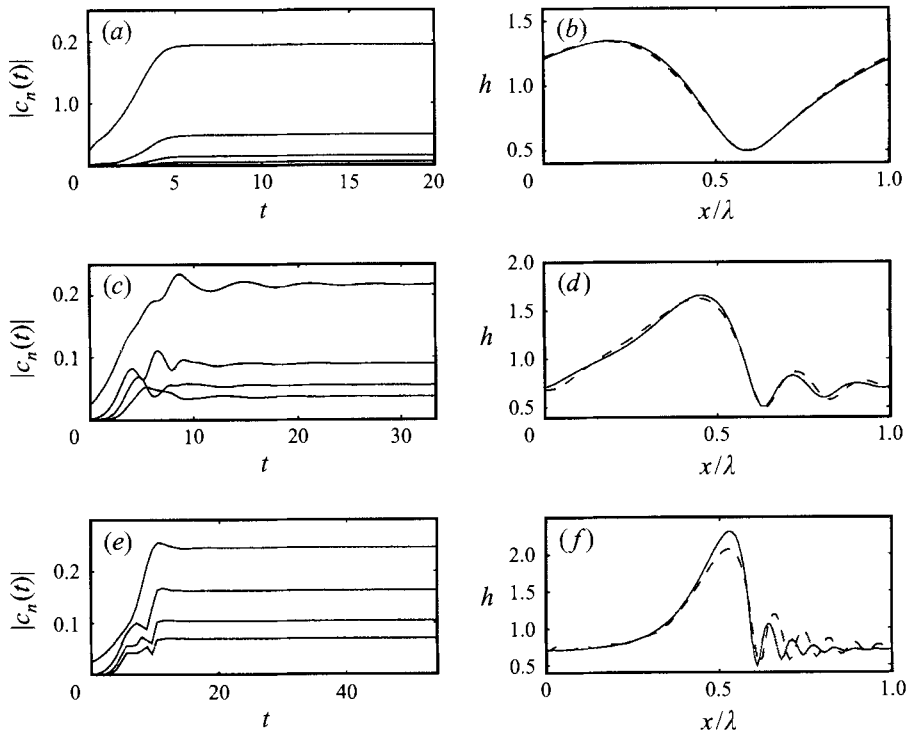

FIGURE 7. $G = 25.0$, $T = 100$, $\beta = \pi/2$: (*a*) evolution of the spectral coefficients for $k = 0.30$ ($\approx k_M$); (*b*) final permanent waveform for $k = 0.30$ ($\approx k_M$); (*c*) evolution of spectral coefficients for $k = 0.15$ ($\approx k_M/2$); (*d*) final permanent waveform for $k = 0.15$ ($\approx k_M/2$); (*e*) evolution of spectral coefficients for $k = 0.075$ ($\approx k_M/4$); and (*f*) final permanent waveform for $k = 0.075$ ($\approx k_M/4$). The wave profiles obtained using the integral boundary layer theory are shown in broken lines.

solitary humps are too closely packed, resulting in interaction between the subsidiary waves and the primary hump. No permanent waveform is observed in this case, but the quasi-periodic behaviour is observed.

The simulations for $G = 5, 25, 100$ also seem to indicate that the band of wavenumbers for which we observe quasi-periodic behaviour increases in size with increasing Reynolds numbers. An extensive parametric search in the range $5 \leqslant G \leqslant 100$, has been performed to obtain the phase diagram shown in figure 10. The transition from finite-amplitude nearly sinusoidal waves to a solitary wave train goes through a transition regime, in which we do not observe periodic waveforms but most likely observe quasi-periodic waveforms. Beyond wave inception, the amplitude of the disturbance grows quickly and saturates due to nonlinear interactions resulting in saturated finite-amplitude waves. This is the primary surface-wave instability in thin-film flows, which is susceptible to secondary subharmonic and sideband instabilities. These secondary instabilities lead to coalescence between the neighbouring peaks, leading to the formation of solitary waves, which are the stable waveform far away from the source (Cheng & Chang 1995). The quasi-periodic behaviour observed in our temporal stability analysis is a manifestation of the secondary sideband instability. As the wavenumbers are reduced further however, a window of stable waveforms reappears due to the secondary subharmonic instability.

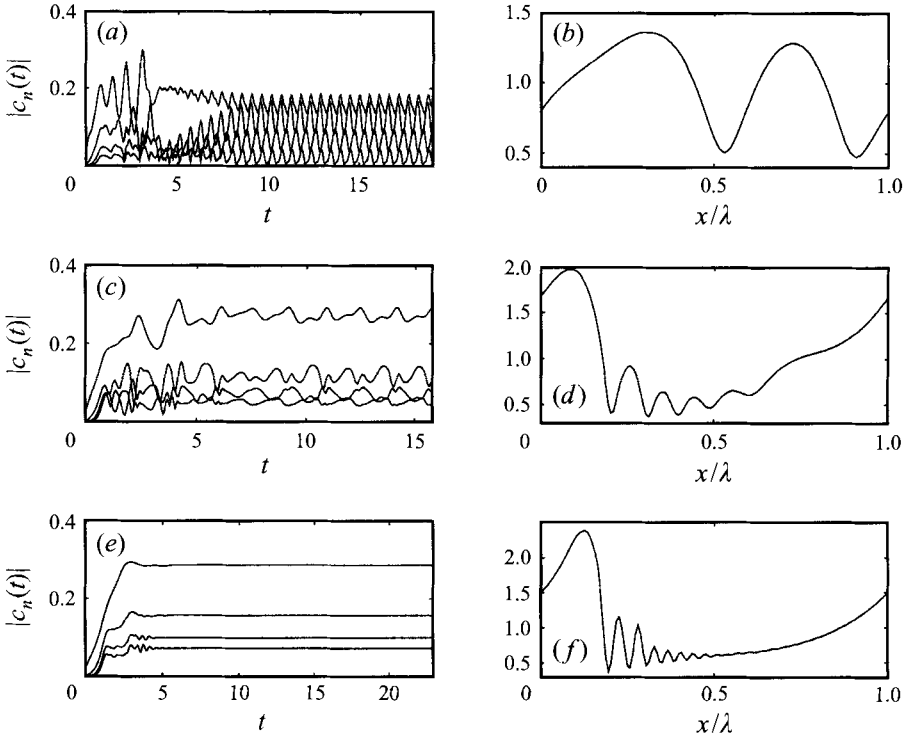

FIGURE 8. $G = 100.0$, $T = 100$, $\beta = \pi/2$: (*a*) evolution of the spectral coefficients for $k = 0.40$ ($\approx k_M$); (*b*) shape of the wave at a particular instant of time for $k = 0.40$ ($\approx k_M$); (*c*) evolution of spectral coefficients for $k = 0.20$ ($\approx k_M/2$); (*d*) shape of the wave at a particular instant of time for $k = 0.20$ ($\approx k_M/2$); (*e*) evolution of spectral coefficients for $k = 0.10$ ($\approx k_M/4$); and (*f*) final permanent waveform for $k = 0.10$ ($\approx k_M/4$).

6. Spatio–temporal evolution of the thin-film instability

In the previous section, we studied the temporal evolution of the surface wave instability in a periodic domain. In reality, the fluid domains are not restricted by periodicity, and the surface wave evolves both spatially as well as temporally, allowing complex wave interactions such as wave mergers and wave splitting. Spatio–temporal evolution of the instability and the wave interaction processes are thus studied in this section.

6.1. *Long domain with periodic boundary conditions*

The parameters are chosen as $G = 5$, $T = 100$, $\beta = \pi/2$, and the length of the streamwise periodic domain is set to $20\lambda_M$. In the first 1/20th of the domain, i.e. for $0 \leqslant x \leqslant \lambda_M$, the equilibrium wave profile (figure 6*b*) computed previously is imposed as the initial condition and the rest of the domain is undisturbed. In the absence of external forcing, the natural waves that evolve downstream of the wave inception are of wavelength λ_M (Chang 1994). This type of initial condition helps us understand how these natural waves evolve further downstream.

The dispersion of the initially imposed wave is shown in figure 11(*a*). The primary surface wave instability being convective in nature, the initial wave is transported downstream. In the process, however, the initial wave disperses into several capillary waves. The front running wave quickly attains the shape of a solitary hump and

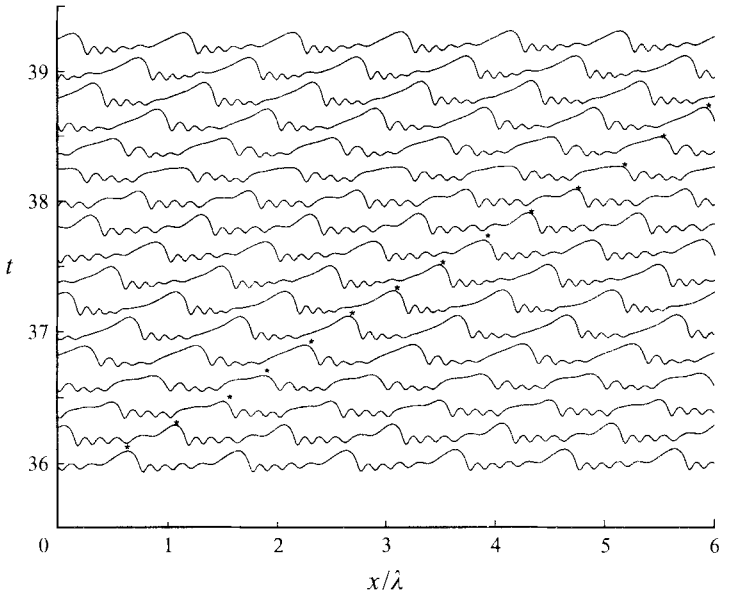

FIGURE 9. $G = 100$, $T = 100$, $k = 0.20$ and $\beta = \pi/2$: free-surface profiles at different instants of time shown in a six-wavelength domain.

travels downstream at a constant velocity and without further generation of waves. Each of the trailing waves as they travel downstream evolves into a solitary waves with sharp downstream slope and a gently sloping tail (figure 11*b*). Thus, very far away from the source, the stable waveform is a solitary waveform. The domain being periodic, the wave leaving the domain at the right enters at the left. The speed of the wave is seen to be proportional to the wave amplitude. This fact was also observed experimentally by Liu & Gollub (1994). The larger-amplitude solitary waves travel faster and run into small capillary waves (figure 11*c*). There does not appear to be any repulsion between the two waves as they come close to each other. At the end of the wave coalescence, a still larger amplitude is formed, which travels downstream leaving behind a quiescent interface devoid of any small-scale ripples. The coalescence between the large-amplitude solitary wave and the relatively smaller-amplitude capillary ripples is thus an inelastic one. This type of wave interactions goes on for a long time, until the only waves seen on the interface are of the solitary-wave type (figure 11*d*). Since the solitary pulses have nearly the same shape and amplitude they all travel with nearly the same speed and no more wave merging or wave splitting phenomena are found to occur. However, there seems to be nonlinear interaction between the solitary pulses which prevents the harmonic modes from settling down to a constant state resulting in a steady travelling solitary wavetrain. Instead, we observe continuous transfer of energy between the various modes resulting in a quasi-periodic behaviour, which was also observed previously in the temporal stability analysis (§5). About $t = 2000$, a solitary wavetrain with 11 solitary pulses is formed in the domain. Even after integrating in time up to $t = 4500$, the number of pulses is found to remain the same, namely 11 in a domain of length $20\lambda_M$ (figure 11*d*). The only changes in the domain are the relative spacing between the different solitary pulses. The solitary pulses are continuously interacting with each other to arrive at an appropriate relative distance. However, the temporal saturation of the solitary wavetrain is not complete

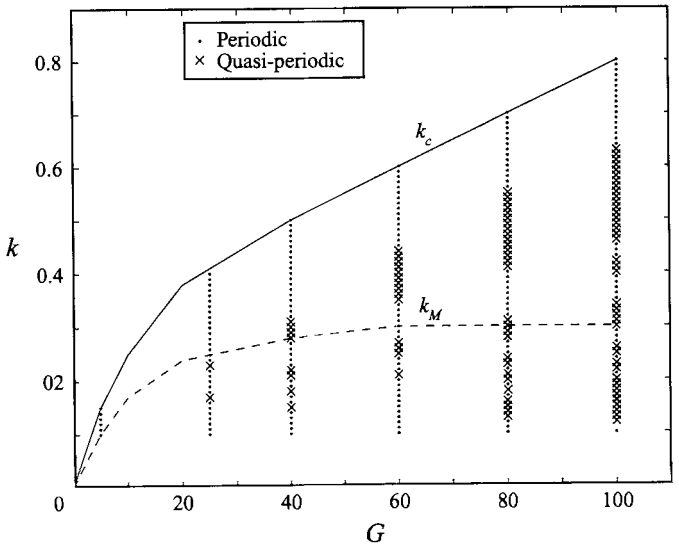

FIGURE 10. Stability diagram for isothermal thin-film flow for $T = 100$ and $\beta = \pi/2$. The cut-off wavenumber k_c and the maximum growth rate wavenumber k_M are taken from Whitaker (1964) who solved the Orr–Sommerfeld equation numerically. Numerical simulations have been performed for $G = 5, 25, 40, 60, 80$ and 100 from $k = k_c$ to $k = 0.10$ in steps of 0.01. The dots represent steady travelling waveforms and the crosses represent quasi-periodic waveforms.

in the numerical integration time $0 \leqslant t \leqslant 4500$. A much longer time of integration may be required before complete temporal saturation can be obtained.

For the same simulation parameters as above, namely $G = 5$, $T = 100$, $\beta = \pi/2$ and a streamwise-periodic domain with length $L = 20\lambda_M$, an exponential pulse of the form $h(x,0) = 1 + 0.05e^{(-0.01(x-L/2)^2)}$ is initially imposed, and its spatio–temporal evolution is studied. The initial dispersion of this disturbance and the evolution into solitary waveform is shown in figure 12(*a*). The spatio–temporal evolution is qualitatively the same as that seen previously, with complicated wave splitting and wave mergers taking place continuously, until a solitary wavetrain is formed (figure 12*b*). The notable difference from the previous simulation is the presence of 13 solitary pulses in the wavetrain in a domain of size $20\lambda_M$. Just as in the previous case, after the formation of a solitary wavetrain with 13 solitary pulses (around $t = 2000$), further integration in time (up to $t = 4355$) is only found to change the relative spacing between the pulses, without changing the number of solitary pulses in the domain. Thus the relative spacing between the solitary pulses, or the natural nonlinear wavelength, is found to be weakly dependent on the initial conditions.

The question of wave breaking in laminar thin film flows is still an open one, and no conclusive theoretical, experimental or numerical evidence on this effect exists to date. The tendency for wave breaking arises from the thickness dependence of the local phase speed, with the crests travelling faster than the troughs resulting in steepening of the wave. The wave interaction processes described in this section could, however, inhibit the wave breaking tendency.

Theoretical interest has focused on determining if the approximate evolution equations such as the Kuramoto–Sivashinsky equation and the long-wave evolution equation of the Benney type admit wave breaking solutions. The Kuramoto–Sivashinsky (KS) equation can accurately model evolution of the surface wave instability in

thin-film flows in the limit of small wave amplitude and large surface tension. The solutions of the KS equation are, however, smooth at all times and do not exhibit any wave breaking tendency. Rosenau & Oron (1989) hypothesized that this is due to the over-prediction of the effect of surface tension in the KS equation and proposed a modification to the curvature term in the KS equation. They retained the higher-order terms in the denominator of the curvature and called their modified KS equation the regularized Kuramoto–Sivashinsky equation (RKS). Through numerical experiments, they show that in certain range of parameters the RKS equation exhibits a wave breaking tendency. Joo & Davis (1991) demonstrate that the long-wave evolution equation of the Benney type (1.2) also exhibits the numerical blowup behaviour. However, both KS and longwave evolution equations are based on the assumption of finite wave amplitude and spatial gradients and lose their validity long before the onset of wave breaking. Thus, it would be interesting to determine if the numerical blowup of these evolution equations really implies wave breaking. The numerical parameters chosen by Rosenau & Oron (1989) are simulated using our full-scale model and the results are shown in figure 13. We find that the harmonic modes eventually saturate implying that finite-amplitude permanent waveforms are the stable solution for these simulation parameters. This is contrary to what has been observed by Rosenau & Oron (1989) in their solution of the RKS equation. The RKS equation thus appears to have no physical relevance.

6.2. *Long domain with non-periodic boundary conditions*

Up to now, all the domains considered are periodic in the streamwise direction, and what is studied is strictly the temporal stability of the thin-film flows. In the experimental studies of thin-film instability, however, a periodic disturbance either in the form of pressure fluctuations or film thickness perturbations is imposed at the inlet and the evolution of this disturbance in the streamwise direction is measured (spatial stability analysis). For infinitesimal disturbances (linear stability), temporal and spatial stability give us equivalent critical conditions. When the disturbances are of finite amplitude (nonlinear stability) this is not always the case, and additional information can be obtained by considering both approaches. In this section, the spatial stability of the thin-film flows is studied numerically in a manner akin to the physical experiments. For this purpose, the experimental conditions of Liu & Gollub (1994) are simulated. They studied the solitary wave dynamics of thin film flows, using a 54% by weight aqueous solution of glycerin and imposing periodic pressure fluctuations at the inlet. The angle of inclination $\beta = 6.4°$; and the mean film thickness is $h_0 = 0.12789$ cm. These experimental conditions correspond to $G = 520.32$, $S = 676.65$, and $T = 84.10$. The film thickness at the inlet is perturbed in the following manner:

$$h(0,t) = 1 + \delta \sin(\omega t), \tag{6.1}$$

where ω and δ are respectively the non-dimensional angular frequency and amplitude of the external periodic forcing. The velocity boundary conditions at the inlet are of the Dirichlet type and are imposed based on the lubrication approximation and in such a way that the continuity equation is satisfied:

$$u(0,y,t) = G \sin\beta \left(h(0,t)y - \frac{y^2}{2} \right), \tag{6.2a}$$

$$v(0,y,t) = \frac{1}{2} \frac{\partial h}{\partial t} \frac{y^2}{2}. \tag{6.2b}$$

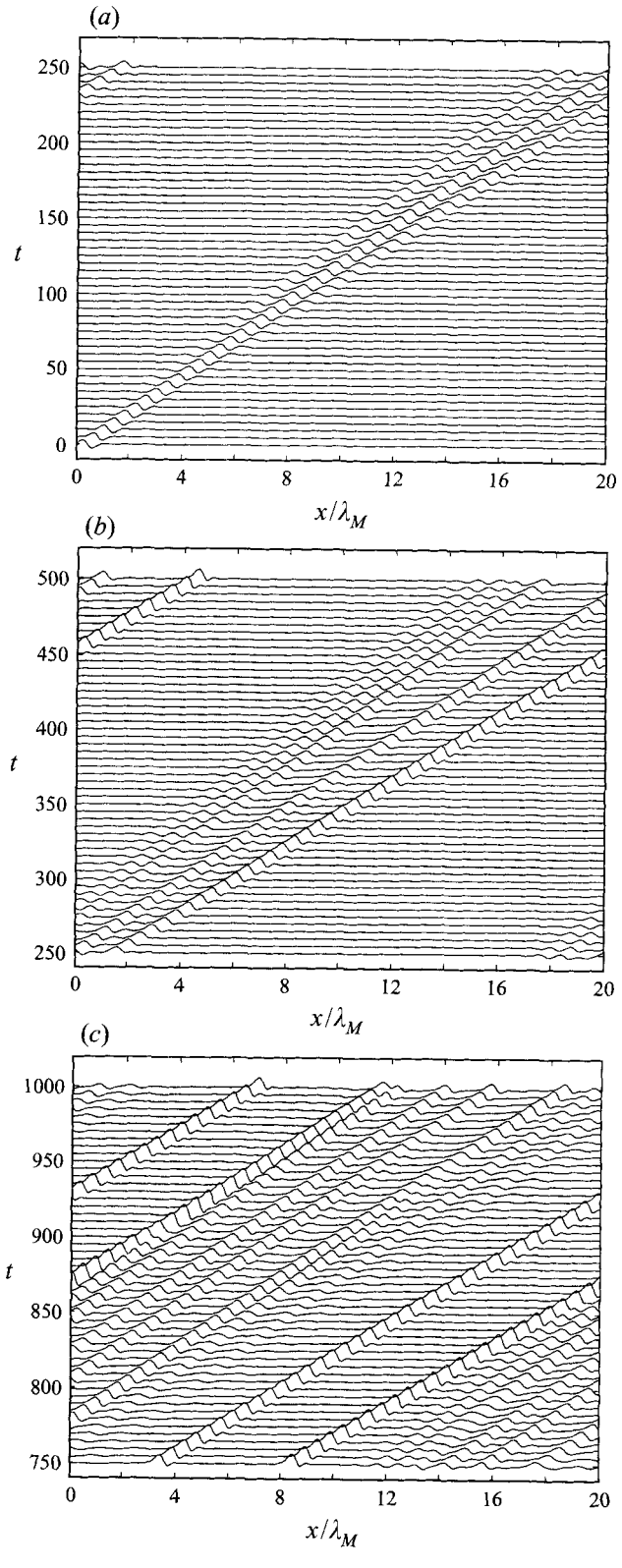

FIGURE 11 (*a–c*). For caption see facing page

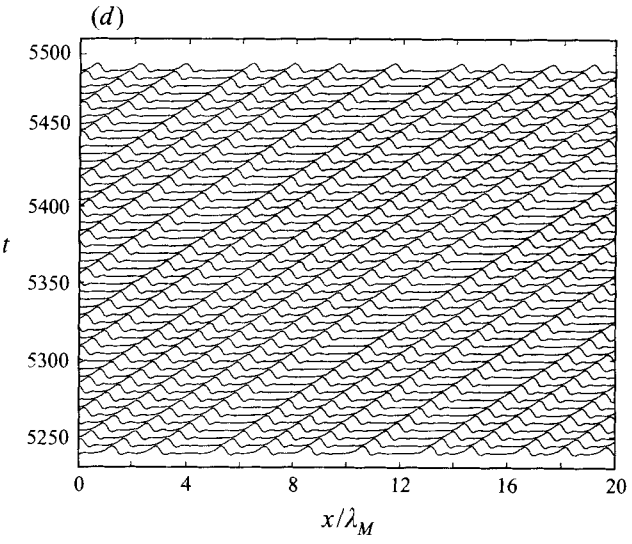

FIGURE 11. $G = 5.0$, $T = 100.0$, $\beta = \pi/2$ and length of the domain $= 20\lambda_M$ with periodic boundary conditions in the streamwise direction. The free-surface profiles shown are in intervals of $\Delta t = 5$. (*a*) $t = 0$ to $t = 250$; (*b*) $t = 250$ to $t = 500$; (*c*) $t = 750$ to $t = 1000$; (*d*) $t = 5240$ to $t = 5490$.

At the exit $x = L$, Sommerfeld radiation boundary conditions are imposed in a manner similar to that proposed by Orlanski (1976) to let the waves leave the computational domain with minimum reflection.

First we present our results corresponding to a 1.5 Hz forcing frequency (figure 3 in Liu & Gollub 1994). The amplitude of the disturbance is set to $\delta = 0.05$. The film thickness $h(x,t)$ at various instants of time from $t = 0$ to $t = 10$ in steps of 0.4 is shown in figure 14(*a*). The primary instability being convective, the disturbance is transported downstream by the mean flow. According to the linear stability theory the cut-off frequency for the onset of instability is $\omega_c = 37.05$. Since the imposed frequency is much smaller than the cut-off frequency, the most likely waveform is a solitary waveform, and that is what is observed. The amplitude of the disturbance quickly grows downstream and the wave becomes asymmetrical, with a sharp upstream slope and a gently trailing tail. Several small-amplitude capillary ripples are formed downstream of the primary hump. In figures 14(*b*) and 14(*c*) the subsequent free surface profiles in steps of 0.4 are shown. The wave travelling at the front grows in amplitude, travels faster and ultimately leaves the computational domain. After the initial growth, the wave profile does not appear to change much in its journey downstream. Thus the gas–liquid interface is filled with solitary humps having teardrop profiles and there appears to be spatial saturation in the waveform. Further downstream however, spatio-temporal chaos and transverse three-dimensional instabilities will set in. The free-surface profile given by Liu & Gollub (1994) is compared to a numerically computed free-surface profile in figure 15. The agreement between the experimental and numerical profiles is not good in the first half of the domain. This is most probably due to a difference in the amplitude of the inlet excitation. The saturated wave profiles in the later part of the domain (figure 15*c*), however, show very good agreement. The significant difference is that the amplitude of the wave as predicted by the numerical calculations is slightly more

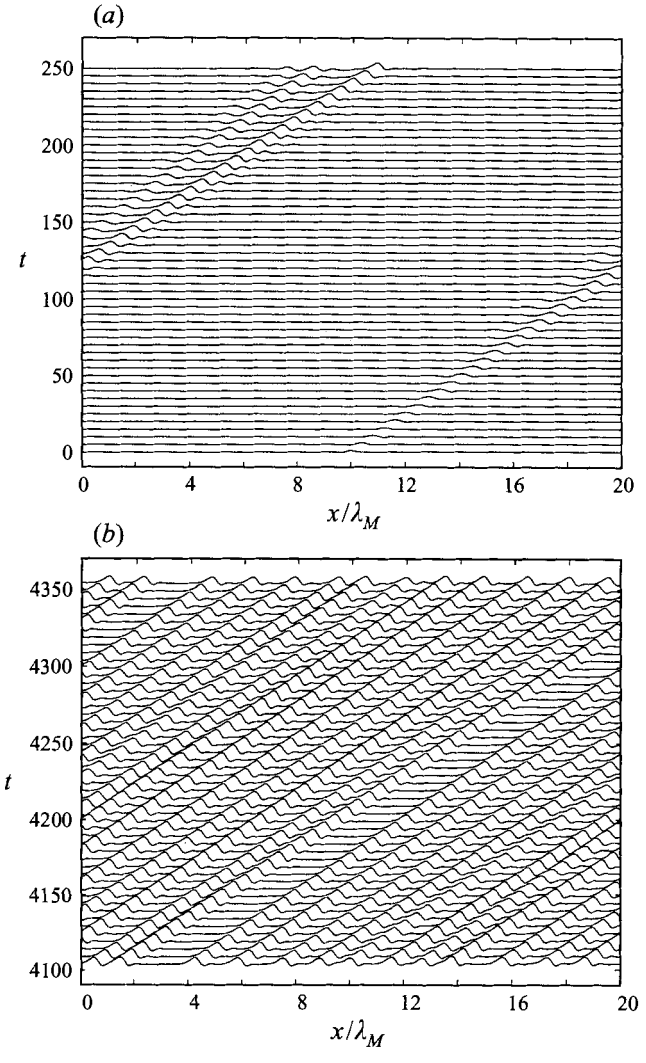

FIGURE 12. $G = 5.0$, $T = 100.0$, $\beta = \pi/2$ and length of the domain $L = 20\lambda_M$, periodic boundary conditions in the streamwise direction and the initial disturbance on the free surface is an exponential disturbance of the form $h(x,0) = 1 + 0.05e^{(-0.01(x-L/2)^2)}$. The free-surface profiles are shown in intervals of $\Delta t = 5$. (*a*) $t = 0$ to $t = 250$; and (*b*) $t = 4105$ to $t = 4355$.

than the experimental value. The capillary ripples downstream of the primary hump are captured quite well by the numerical solution.

The experimental conditions simulated next are same as the above except that the inlet forcing frequency is increased to 4.5 Hz and the amplitude of the excitation is taken to be $\delta = 0.01$. The free-surface profiles in time-steps of 0.4 are shown in figure 16(*a–c*). The inlet forcing frequency controls the spacing between the solitary humps. In this case the frequency is quite high and the solitary humps are too close to each other and never settle down to achieve steady travelling waveforms. This is analogous to the quasi-periodic behaviour we observed for some wavenumbers in the study of temporal instability. The experimental and numerical wave profiles are compared in figure 17. Just as in the previous case, the agreement is not very good

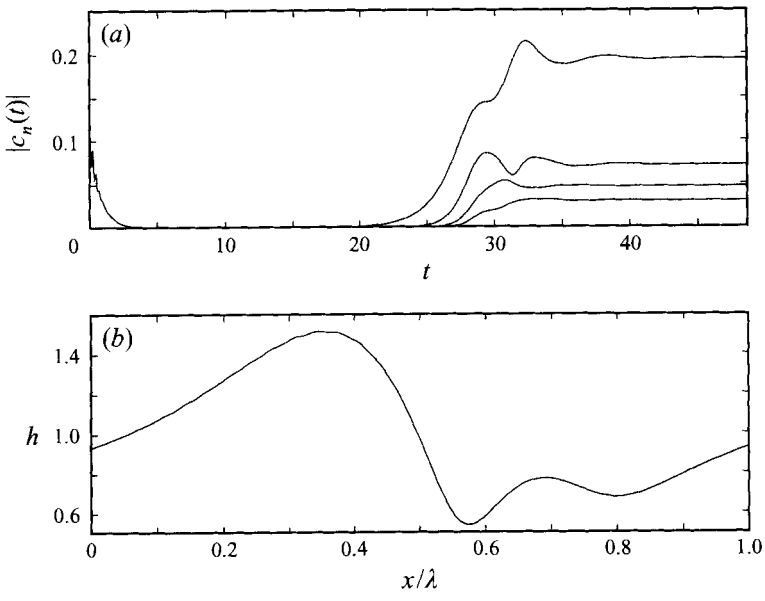

FIGURE 13. Rosenau & Oron (1989)'s wave breaking simulation with simulation parameters $G = 16.0$, $S = 51.63$, $\beta = \pi/2$ and $k = 0.2783$.

in the first part of the domain (figure 17*a*). This either due to a difference in the forcing amplitude at the inlet or due to a difference in the way the flow is excited at the inlet. Liu & Gollub (1994) impose fluctuations in the pressure, where as in the numerical simulations the film thickness is excited. In the later part of the domain the agreement is very good (figure 17*b*, *c*). Since the solitary waves are too closely packed we do not observe spatial saturation.

Lastly, keeping the same experimental conditions as above, but increasing the inlet forcing frequency to 7 Hz, we obtain nearly sinusoidal film profiles as shown in figure 18. The waves are closely packed, nearly sinusoidal and symmetrical. The forcing frequency in this case is close to the cut-off frequency, hence the almost sinusoidal wave profile. The comparison with experiments is very good in this case also (figure 18*b*, *c*).

In §4, the experimental conditions of Kapitza & Kapitza (1949) were simulated numerically in a periodic domain. For one of the experimental conditions (figures 4,5), our full-scale numerical simulations predict a quasi-periodic waveform in contrast to the periodic waveforms reported by Kapitza & Kapitza (1949). The same experimental conditions are now numerically simulated in a long non-periodic domain and the spatial evolution of the disturbance is simulated in a manner similar to the physical experiments; the results are shown in figure 19. No spatial saturation is observed in the stream-wise direction and the wave profile is quasi-periodic consistent with the temporal stability predictions.

7. Concluding remarks

Extensive numerical simulations based on the direct solution of the Navier–Stokes equations reveal some interesting features of the thin-film instability. In concurrence with what is known about thin-film instability based on linear and approximate non-

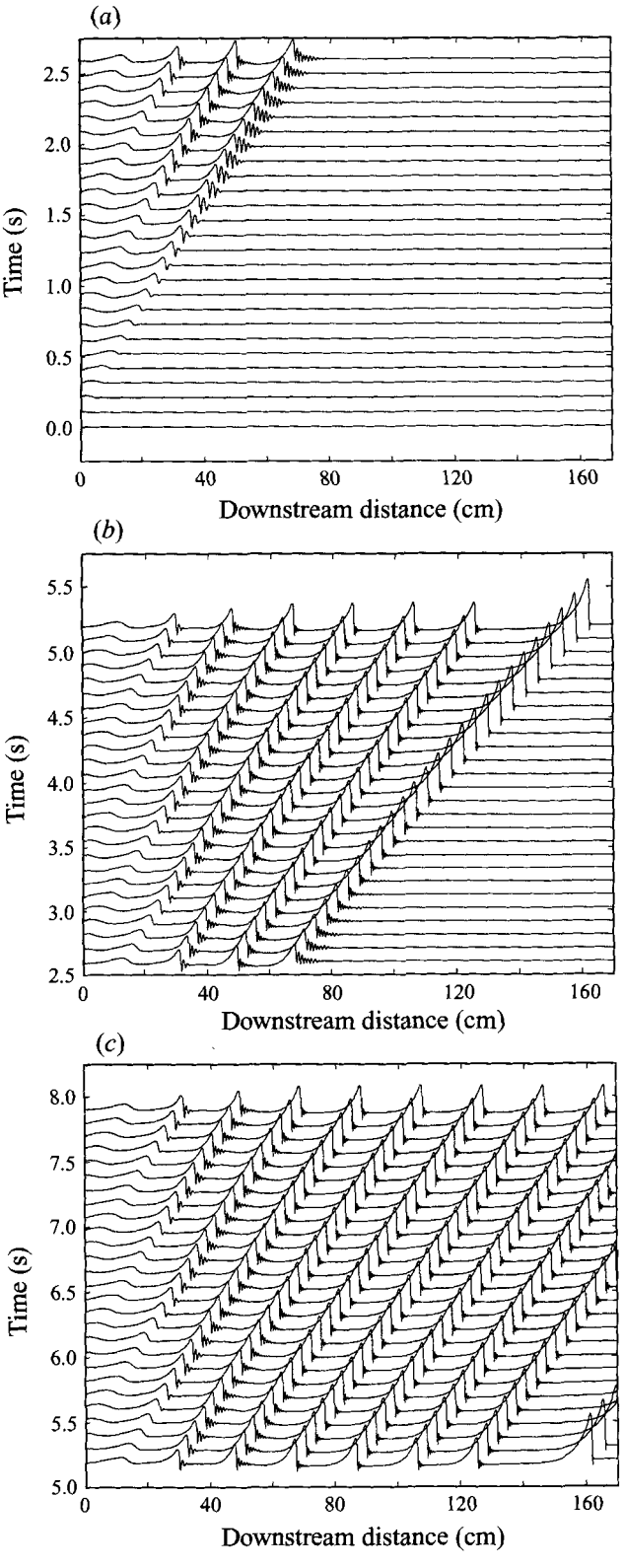

FIGURE 14. For caption see facing page

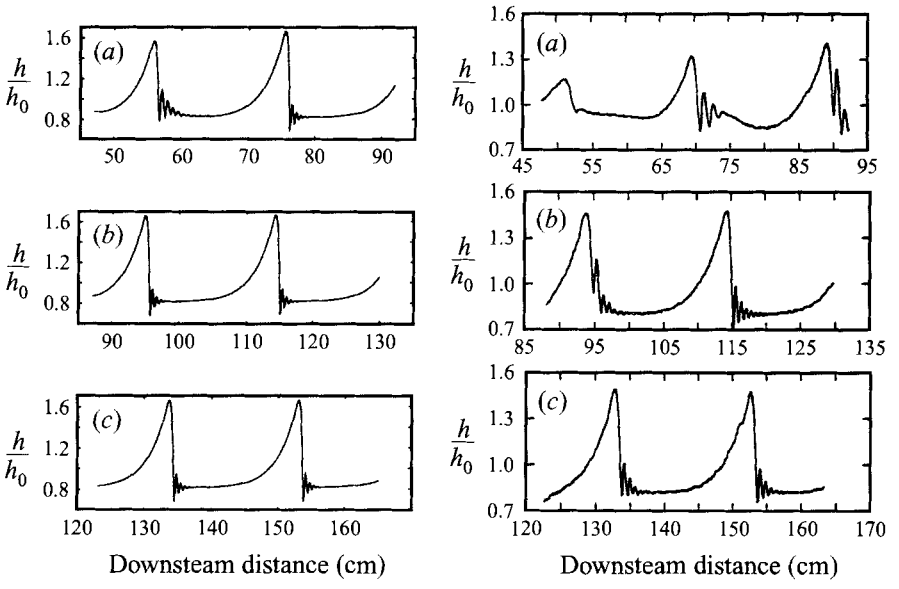

FIGURE 15. $G = 520.32$, $S = 676.65$, $\beta = 6.4°$ and corresponds to the experimental conditions of Liu & Gollub (1994) (figure 3). A sinusoidal perturbation of the form $h(0,t) = 1+0.05\sin(2.4546t)$ is imposed at the inlet. The wave profiles (h/h_0 versus x) shown on the left are obtained computationally and the ones shown at the right are those measured by Liu & Gollub (1994) (figure 3).

linear theories, finite-amplitude waveforms are the stable solution for wavenumbers smaller than the linear cut-off wavenumber k_c. For wavenumbers close to k_c, the waveforms are nearly sinusoidal. For wavenumbers much smaller than k_c, the waveforms are solitary-wave-like. This transition from nearly sinusoidal waveforms to solitary waveforms seem to pass through a quasi-steady regime, in which the spatial harmonic coefficients are in a state of constant fluctuations. The phase boundary delineating this regime has been obtained through extensive numerical simulations.

Comparison between the full-scale computations and approximate nonlinear theories indicates that these theories are accurate in the parametric regimes for which they are derived. Since only a very small number of comparisons have been made it was not possible to derive definite boundaries delineating the regimes where the approximate nonlinear theories are accurate. Both the Reynolds number G and the surface tension parameter T influence the accuracy of the approximate nonlinear theories. For moderate surface tension ($T = 100$) and vertically draining film, the lubrication theory of the Benney type (1.2) was found to give accurate predictions for $G = 5$ and the integral boundary layer theory (1.4) was found to give accurate predictions for $G = 25$. However, for $G = 100$, the integral boundary layer theory based on a parabolic velocity profile and hydrostatic pressure approximation (1.4) could not be solved. A more accurate boundary layer theory such as the one developed by Lee & Mei (1995) retaining the higher-order terms in the hydrostaic pressure approximation

FIGURE 14. $G = 520.32$, $S = 676.65$, $\beta = 6.4°$ and corresponds to the experimental conditions of Liu & Gollub (1994) (figure 3). A sinusoidal perturbation of the form $h(0,t) = 1 + 0.05 * \sin(2.4546t)$ is imposed at the inlet. The free-surface profiles shown are shown in intervals of 0.104 s from: (*a*) $t = 0$ to $t = 2.60$ s; (*b*) $t = 2.60$ s to $t = 5.20$ s; (*c*) $t = 5.20$ s to $t = 7.80$ s.

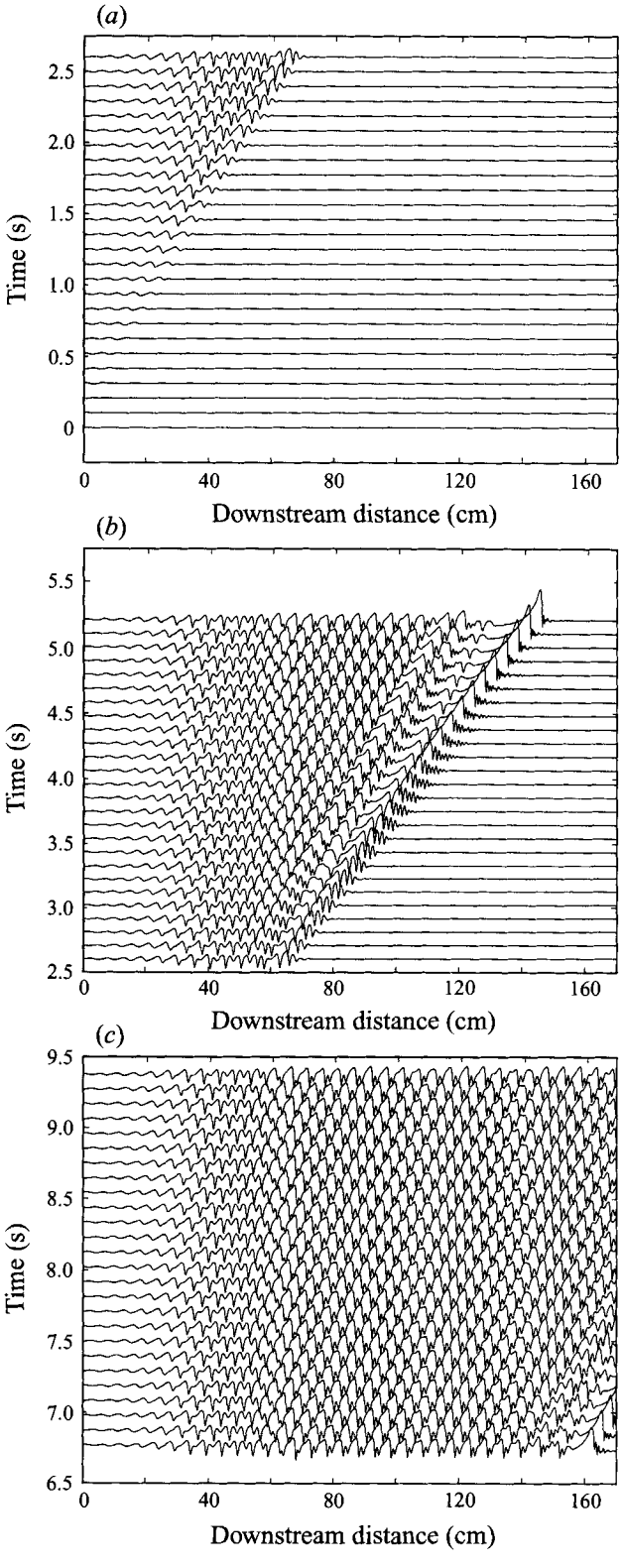

FIGURE 16. For caption see facing page.

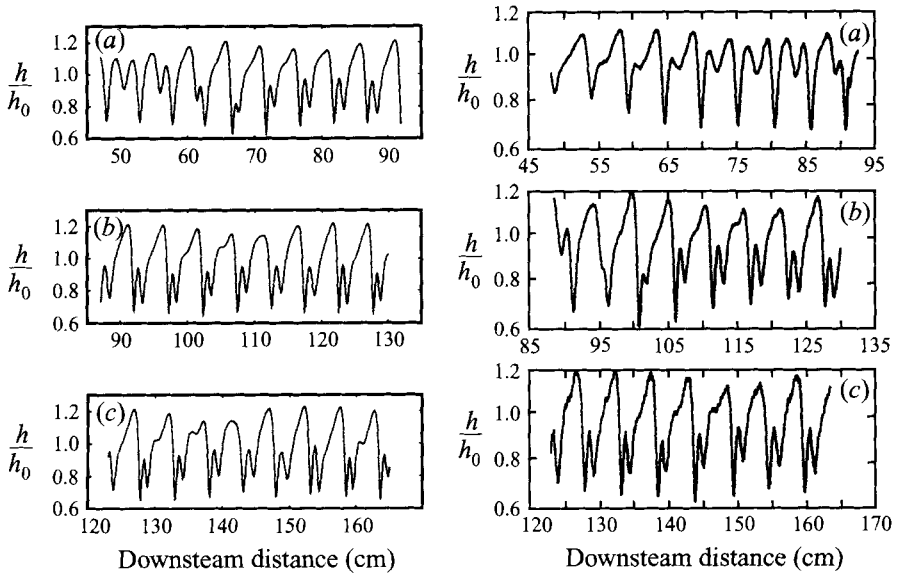

FIGURE 17. $G = 520.32$, $S = 676.65$, $\beta = 6.4°$ and corresponds to the experimental conditions of Liu & Gollub (1994) (figure 7). A sinusoidal perturbation of the form $h(0,t) = 1+0.05\sin(7.3638t)$ is imposed at the inlet. The wave profiles (h/h_0 versus x) shown on the left are obtained computationally and the ones shown at the right are those measured by Liu & Gollub (1994) (figure 7).

may have to be used in this range of parameters. However, in the event of large wave amplitude and/or wave steepening, none of the appproximate nonlinear theories can be used, and experiments or full-scale computations based on the solution of the complete Navier–Stokes equations will need to be used.

The spatial stability analysis of the thin-film instability has also been studied by considering a very long domain with periodic forcing at the inlet and absorbing boundary conditions at the exit. Very good agreement with the experiments of Liu & Gollub (1994) has been obtained. Depending on the frequency of excitation, the waves formed downstream are either nearly sinusoidal or solitary-like or quasi-periodic.

Owing to the amplitude dependence of the wave speed, complex wave interactions are likely to occur on the gas–liquid interface. Waves with larger amplitude travel faster and coalesce with smaller waves. This wave interaction is found to be completely inelastic and the resultant wave grows further in amplitude and travels downstream leaving behind a nearly flat interface. However, there appears to be a natural wavelength that the system tries to achieve in the solitary wave regime. The resultant wavelength downstream is also weakly dependent on the initial condition.

A powerful numerical technique has been developed and applied to the study of surface wave instability in isothermal thin-film flows. A natural extension of the numerical procedure would be to do three-dimensional simulations. Very far away from

FIGURE 16. $G = 520.32$, $S = 676.65$, $\beta = 6.4°$ and corresponds to the experimental conditions of Liu & Gollub (1994) (figure 7). A sinusoidal perturbation of the form $h(0,t) = 1 + 0.01\sin(7.3638t)$ is imposed at the inlet. The free-surface profiles are shown in intervals of 0.104 s from: (*a*) $t = 0$ to $t = 2.60$ s; (*b*) $t = 2.60$ s to $t = 5.20$ s; and (*c*) $t = 6.656$ s to $t = 9.40$ s.

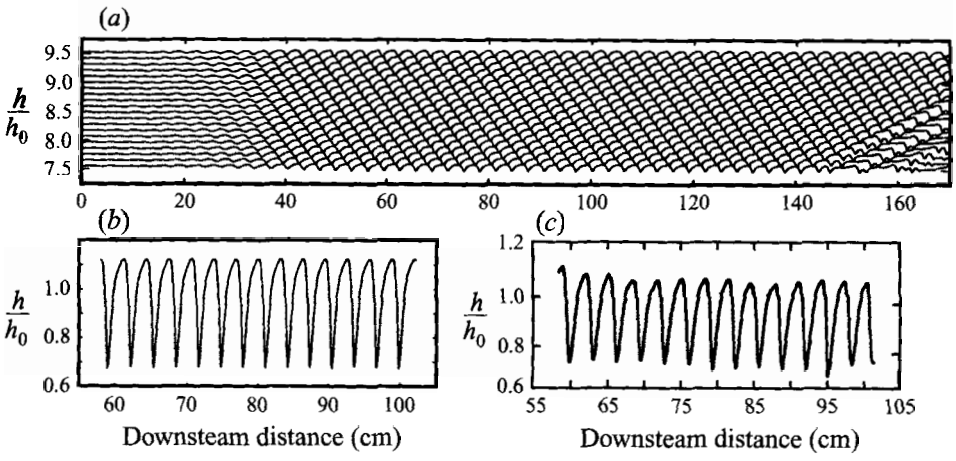

FIGURE 18. $G = 520.32$, $S = 676.65$, $\beta = 6.4°$ and corresponds to the experimental conditions of Liu & Gollub (1994) (figure 8). A sinusoidal perturbation of the form $h(0,t) = 1 + 0.05\sin(11.4548t)$ is imposed at the inlet. (*a*) Film thicknesses in intervals of 0.104 s from $t = 7.6$ s to $t = 9.6$ s; (*b*) numerically computed free surface profile (h/h_0 versus x); and (*c*) experimentally reported film thickness profile (h/h_0 versus x) (figure 8 in Liu and Gollub 1994).

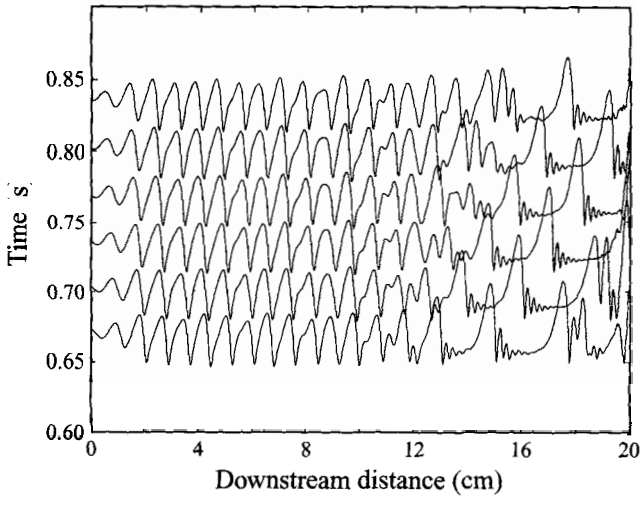

FIGURE 19. $G = 60.0$, $S = 4410$, $\beta = \pi/2$ and $\omega = 5.707$. At the inlet the free surface is perturbed as follows: $h(0,t) = 1 + \delta\sin(\omega t)$. The free-surface profiles in steps of 0.033 s are shown.

the source the nonlinear waves are three-dimensional. A numerical procedure based on the direct solution of the three-dimensional Navier–Stokes equations would help us understand this nonlinear wave regime. Krishnamoorthy (1996) has already done some three-dimensional numerical studies of both isothermal and heated thin-film flows and addressed the question of rupture and rivulet formation. Liu, Schneider & Gollub (1995) have done a detailed experimental study of three-dimensional instabilities. It would be very interesting to perform direct numerical simulation of three-dimensional instabilities and make comparisons with the experimental observations of Liu *et al.* (1995).

The authors acknowledge the support for this work provided by NSF, under GRANT No. CTS-9408409. Appreciation is expressed to the North Carolina Supercomputing Center for use of their computer facilities. Furthermore, the authors are in debt to the reviewers for their many suggestions.

REFERENCES

ALEKSEENKO, S. V., NAKORYAKOV, V. YE. & POKUSAEV, B. G. 1985 Wave formation on a vertical falling liquid film. *AIChE J.* **31**, 1446–1460.

AMSDEN, A. A. & HIRT, C. W. 1973 YAQUI: an arbitrary Lagrangian–Eulerian computer program for fluid at at all speeds. *Los Alamos Scientific Lab. Report*, LA-5100.

ANSHUS, B. E. & GOREN, S. L. 1964 A method of getting approximate solutions to the Orr–Sommerfeld equation for flow on a vertical wall. *AIChE J.* **12**, 1004–1008.

BACH, P. & VILLADSEN, J. 1984 Simulation of the vertical flow of a thin, wavy film using a finite element method. *Intl J. Heat Mass Transfer* **27**, 815–827.

BEHR, M. A., FRANCA, L. P. & TEZDUYAR, T. E. 1992 Stabilized finite element methods for the velocity–pressure–stress formulation of incompressible flows. *University of Minnesota Supercomputer Institute Research Rep.* UMSI 92/8.

BELL, J. B., COLELLA, P. & GLAZ, H. M. 1989 A second-order projection method for the incompressible Navier–Stokes equations. *J. Comput. Phys.* **85**, 257–283.

BELYTSCHKO, T. B. & FLANAGAN, D. P. 1982 Finite element methods with user controlled meshes for fluid–structure interaction. *Comput. Meth. Appl. Mech. Engng* **33**, 669–688.

BENJAMIN, T. B. 1957 Wave formation in laminar flow down an inclined plane. *J. Fluid Mech.* **2**, 554–574.

BENNEY, D. J. 1966 Long waves on liquid films. *J. Math. Phys.* **45**, 150–155.

BRAUNER, N. & MARON, D. M. 1982 Characteristics of inclined thin films. Waviness and the associated mass transfer. *Intl J. Heat Mass Transfer* **25**, 99–110.

CHAN, R. K.-C. 1975 A generalized arbitrary Lagrangian Eulerian method for incompressible flows with sharp interfaces. *J. Comput. Phys.* **17**, 311-331.

CHANG, H.-C. 1994 Wave evolution on a falling film. *Ann. Rev. Fluid Mech.* **26**, 103–136.

CHANG, H.-C., DEMEKHIN, E. A. & KOPELEVICH, D. I. 1993 Nonlinear evolution of waves on a vertically falling film. *J. Fluid Mech.* **250**, 433–480.

CHENG, M. & CHANG, H.-C. 1995 Competition between subharmonic and sideband secondary instabilities on a falling film. *Phys. Fluids* **7**, 34–54.

CHIN, R. W., ABERNATHY, F. F. & BERTSCHY, J. R. 1986 Gravity and shear wave stability of free surface flows. Part 1. Numerical calculations. *J. Fluid Mech.* **168**, 501–513.

CHORIN, A. J. 1967 A numerical method for solving viscous incompressible flow problems. *J. Comput. Phys.* **2**, 12–26.

DONEA, J. 1983 Arbitrary Lagrangian Eulerian finite element methods. In *Computational Methods for Transient Analysis* (ed. T. B. Belytschko & T. J. R. Hughes), pp. 474–516. John Wiley & Sons.

DONEA, J., GIULIANI, S. & LAVAL, H. 1982*a* Finite element solution of the unsteady Navier–Stokes equations by fractional step method. *Comput. Meth. Appl. Mech. Engng* **30**, 53–73.

DONEA, J., GIULIANI, S. & HALLEUX, J. P. 1982*b* An arbitrary Lagrangian Eulerian finite element method for transient dynamic fluid–structure interactions. *Comput. Meth. Appl. Mech. Engng* **33**, 689–723.

DRESSLER, R. F. 1949 Mathematical solution of the problem of roll-waves in inclined open channels. *Commun. Pure Appl. Maths* **2**, 149–194.

FINLAYSON, B. A. 1992 *Numerical Methods for Problems with Moving Fronts*, pp. 434–456. Ravenna Park Publishing Inc., Seattle.

GJEVIK, B. 1970 Occurrence of finite-amplitude surface waves on falling liquid films. *Phys. Fluids* **13**, 1918–1925.

GLOWINSKI, R. 1986 Splitting methods for the numerical solution of the incompressible Navier–Stokes equations. In *Vistas in Applied Mathematics, Optimization and Software* (ed. A. V. Balakrishna *et al.*), pp. 57–95.

GRESHO, P. M. 1990 On the theory of semi-implicit projection methods for viscous incompressible

flow and its implementation via a finite element method that also introduces a nearly–consistent mass matrix Part 1: Theory. *Intl J. Numer. Meth. Fluids* **11**, 587–620.

GRESHO, P. M. 1991 Incompressible fluid dynamics: some fundamental formulation issues. *Ann. Rev. Fluid Mech.* **23**, 413–453.

GRESHO, P. M. & CHAN, S. T. 1990 On the theory of semi-implicit projection methods for viscous incompressible flow and its implementation via a finite element method that also introduces a nearly–consistent mass matrix Part 2: Implementation. *Intl J. Numer. Meth. Fluids* **11**, 621–660.

GRESHO, P. M., CHAN, S. T., CHRISTON, M. A. & HINDMARSH, A. C. 1994 A little more on stabilized Q_1Q_1 for transient viscous incompressible flow. In *Proc. Intl Conf. on Monsoon Variablity and Prediction, Trieste, Italy.*

HIRT, C. W., AMSDEN, A. A. & COOK, J. L. 1974 An arbitrary Lagrangian–Eulerian computing method for all flow speeds. *J. Comput. Phys*, **14**, 227–253.

HO, L.-W. & PATERA, A. T. 1990 A Legendre spectral element method for simulation of unsteady incompressible viscous free-surface flows. *Comput. Meth. Appl. Mech. Engng* **80**, 355–366.

HOOPER, A. P. & GRIMSHAW, R. 1985 Nonlinear instability at the interface between two viscous fluids. *Phys. Fluids* **28**, 37–45.

HUERTA, A. & LIU, W. K. 1988 Viscous flow with large free surface motion. *Comput. Meth. Appl. Mech. Engng* **69**, 277–324.

HUGHES, T. J. R., LIU, W. K. & ZIMMERMAN, T. 1981 Lagrangian–Eulerian finite element formulation for incompressible viscous flow. *Comput. Meth. Appl. Mech. Engng* **29**, 329–349.

JOO, S. W. 1995 *Surface Wave Instabilities in Thin Films.* World Scientific Publishing Co (in press).

JOO, S. W. & DAVIS, S. H. 1991 On falling–film instabilities and wave breaking. *Phys. Fluids* A **3**, 231–232.

JOO, S. W. & DAVIS, S. H. 1992 Irregular waves on viscous falling films. *Chem. Engng Commun.* **118**, 111–123.

JOO, S. W., DAVIS, S. H. & BANKOFF, S. G. 1991 Long-wave instabilities of heated falling films: two-dimensional theory of uniform layers. *J. Fluid Mech.* **230**, 117–146.

KAPITZA, P. L. & KAPITZA, S. P. 1949 Wave flow of thin layers of a viscous fluid:III. Experimental study of undulatory flow conditions. *Zh. Exp. Teor. Fiz.* **19**, 105. Also in *Collected Papers of P. L. Kapitza* (ed. D. Ter Haar), vol. 2, pp. 690–709, Pergamon (1965).

KAWAHARA, M. & OHMIYA, K. 1985 Finite element analysis of density flow using the velocity correction method. *Intl J. Numer. Meth. Fluids* **5**, 981–993.

KHESHGI, H. S. & SCRIVEN, L. E. 1987 Disturbed film flow on a vertical plate. *Phys. Fluids* **30**, 990–997.

KIM, J. & MOIN, P. 1985 Application of a fractional–step method to incompressible Navier–Stokes equations. *J. Comput. Phys.* **59**, 308–323.

KNANI, S. & BANKOFF, G. 1993 Experimental confirmation of Yih–Benjamin linear stability theory for a falling film on a vertical pipe. *J. Israel. Inst. Chem. Engng* **22**, 58–61.

KRANTZ, W. B. & GOREN, S. L. 1971 Stability of thin liquid films flowing down a plane. *Indust. Engng Chem. Fundam.* **10**, 91–101.

KRSIHNAMOORTHY, S. 1996 Instabilities in heated falling films: a full-scale direct numerical simulation. Ph.D. thesis, Mechanical Engineering, Rice University, Houston, TX.

LACY, C. E., SHEINTUCK, M. & DUKLER, A. E. 1991 Methods of deterministic chaos applied to the flow of thin wavy films. *AIChE J.* **37**, 481–489.

LE, H. & MOIN, P. 1991 An improvement of fractional step method for the incompressible Navier–Stokes equations. *J. Comput. Phys.* **92**, 369–379.

LEE, J.-J. & MEI, C. C. 1996 Stationary waves on an inclined sheet of viscous fluid at high Reynolds and moderate Weber numbers. *J. Fluid Mech.* **307**, 191–229.

LIN, S. P. 1969 Finite amplitude stability of a parallel flow with a free surface. *J. Fluid Mech.* **36**, 113–126.

LIN, S. P. & WANG, C. Y. 1985 Modeling wavy film flows. In *Encyclopedia of Fluid Mechanics* (ed. N. P. Chermemisinoff), vol. 1, pp. 931–951. Gulf.

LIU, J. & GOLLUB, J. P. 1993 Onset of spatially chaotic waves on flowing films. *Phys. Rev. Lett.* **70**, 2289–2292.

LIU, J. & GOLLUB, J. P. 1994 Solitary wave dynamics of film flows. *Phys. Fluids* **6**, 1702–1712.

LIU, J., PAUL, J. D. & GOLLUB, J. P. 1993 Measurements of the primary instabilities of film flows. *J. Fluid Mech.* **250**, 69–101.

LIU, J., SCHNEIDER, J. B. & GOLLUB, J. P. 1995 Three dimensional instabilities of film flows. *Phys. Fluids* **7**, 55–67.

LIU, W. K., CHANG, H., CHEN, J. & BELYTSCHKO, T. 1988 Arbitrary Lagrangian Eulerain Petrov–Galerkin finite elements for for nonlinear continua. *Comput. Meth. Appl. Mech. Engng* **68**, 259–310.

MALAMATARIS, N. T., & PAPANASTASIOU, T. C. 1991 Unsteady free surface flows on truncated domains. *Indust. Engng Chem. Res.* **30**, 2211–2219.

MIZUKAMI, A. & TSUCHIYA, M. 1984 A finite element method for the three-dimensional non-steady Navier–Stokes equations. *Intl J. Numer. Meth. Fluids* **4**, 349–357.

NAKAYA, C. 1975 Long waves on a thin fluid layer flowing down an inclined plane. *Phys. Fluids* **18**, 1407–1412.

NUSSELT, W. Die oberflächenkondensation des wasserdampfes. *Z. Ver. Deut. Ing.* **60**, 541–569.

ODEN, J. T. 1992 Theory and implementation of high-order adaptive hp methods for analysis of incompressible viscous flows. In *Computational Nonlinear Mechanics in Aerospace Engineering* (ed. S. N. Atluri), pp. 321–363. AIAA.

ORLANSKI, I. 1976 A simple boundary condition for unbounded hyperbolic flows. *J. Comput. Phys.* **21**, 251–269.

PATANKAR, S. V. 1980 *Numerical Heat Transfer and Fluid Flow.* Hemisphere.

PIERSON, F. W. & WHITAKER, S. 1977 Some theoretical and experimental observations of the wave structure of falling liquid films. *Indust. Engng Chem. Fundam.* **16**, 401–408.

PIRONNEAU, O. 1982 On the transport–diffusion algorithm and its applications to the Navier–Stokes equations. *Numerische Mathematic* **38**, 309–332.

PORTALSKI, S. & CLEGG, A. J. 1972 An experimental study of wave inception on falling liquid films. *Chem. Engng Sci.* **27**, 1257–1265.

PRACHT, W. E. 1975 Calculating three-dimensional fluid flows at all speeds with an Eulerian–Lagrangian computing mesh. *J. Comput. Phys.* **17**, 132–159.

PROKOPIOU, TH., CHENG, M. & CHANG, H.-C. 1991 Long waves on inclined films at high Reynolds number. *J. Fluid Mech.* **222**, 665–691.

PUMIR, A., MANNEVILLE, P. & POMEAU, Y. 1983 On solitary waves running down an inclined plane. *J. Fluid Mech.* **135**, 27–50.

RAMASWAMY, B., JUE, T. C. & AKIN, J. E. 1992 Semi-implicit and explicit finite element schemes for coupled fluid/thermal problems. *Intl J. Numer. Meth. Engng* **34**, 675–696.

RAMASWAMY, B. & KAWAHARA, M. 1987*a* An equal order velocity pressure finite element formulation for solving the time-dependent incompressible Navier–Stokes equations. *Bull. Facul. Sci. Engng Chuo Univ.* **30**, 63–104.

RAMASWAMY, B. & KAWAHARA, M. 1987*b* Arbitrary Lagrangian–Eulerian finite element method for unsteady, convective, incompressible viscous free surface fluid flow. *Intl J. Numer. Meth. Fluids* **7**, 1053–1075.

RICE, J. G. & SCHNIPKE, R. J. 1986 An equal-order velocity–pressure formulation that does not exhibit spurious pressure modes. *Comput. Meth. Appl. Mech. Engng* **58**, 135–149.

ROSENAU, P. & ORON, A. 1989 Evolution and breaking of liquid film flowing on a vertical cylinder. *Phys. Fluids* A **1**, 1763–1766.

ROSKES, G. J. 1970 Three-dimensional long waves on a liquid film. *Phys. Fluids* **13**, 1440–1445.

SAITO, H. & SCRIVEN, L. E. 1981 Study of the coating flow by the finite element method. *J. Comput. Phys.* **42**, 53–76.

SALAMON, T. R., ARMSTRONG, R. C. & BROWN, R. A. 1994 Travelling waves on vertical films: Numerical analysis using the finite element method. *Phys. Fluids* **6**, 2202–2220.

SCHNEIDER, G. E., RAITHBY, G. D. & YOVANOVICH, M. M. 1978 Finite-element solution procedures for solving the incompressible, Navier–Stokes equations using equal order variable interpolation. *Numer. Heat Transfer* **1**, 443–451.

SHAW, C. T. 1991 Using a segregated finite element scheme to solve the incompressible Navier–Stokes equations. *Intl J. Numer. Meth. Fluids* **12**, 81–92.

SIVASHINSKY, G. I. & MICHELSON, D. M. 1980 On the irregular wavy flow of liquid film down a vertical plane. *Prog. Theor. Phys.* **63**, 2112.

SOULAÏMANI, A., FORTIN, M., DHATT, G. & OUELLET, Y. 1991 Finite element simulation of two- and three-dimensional free surface flows. *Comput. Meth. Appl. Mech. Engng* **86**, 265–296.

TEMAM, R. 1971 *On the Theory and Numerical Analysis of the Navier–Stokes Equations.* North-Holland.

WHITAKER, S. 1964 Effect of surface active agents on stability of falling liquid films. *Indust. Engng Chem. Fundam.* **3**, 132–142.

VAN KAN, J. 1986 A second-order accurate pressure correction scheme for viscous incompressible flow. *SIAM J. Sci. Statist. Comput.* **7**, 870–891.

YIH, C.-S. 1955 Stability of parallel laminar flow with a free surface. *Proc. 2nd US Congr. Appl. Mech.*, pp. 623–628. ASME.

YIH, C.-S. 1963 Stability of liquid flow down an inclined plane. *Phys. Fluids* **6**, 321–324.

ZIENKIEWICZ, O. C. & WU, J. 1991 Incompressibility without tears – how to avoid restriction of mixed formulation. *Intl J. Numer. Meth. Engng* **34**, 1189–1203.

ZIENKIEWICZ, O. C. & WU, J. 1992 A general explicit or semi-explicit algorithm for compressible and incompressible flows. *Intl J. Numer. Meth. Engng* **35**, 457–479.